Production of warm dense water in the laboratory using intense ion beams at FAIR: Application to planetary physics

Cite as: Phys. Plasmas **28**, 032712 (2021); https://doi.org/10.1063/5.0037943
Submitted: 18 November 2020 • Accepted: 20 February 2021 • Published Online: 22 March 2021

N. A. Tahir, A. Shutov, P. Neumayer, et al.

Physics of Plasmas ARTICLE scitation.org/journal/php

Production of warm dense water in the laboratory using intense ion beams at FAIR: Application to planetary physics

Cite as: Phys. Plasmas **28**, 032712 (2021); doi: 10.1063/5.0037943
Submitted: 18 November 2020 · Accepted: 20 February 2021 ·
Published Online: 22 March 2021

N. A. Tahir,[1,a)] A. Shutov,[2] P. Neumayer,[1] V. Bagnoud,[1] A. R. Piriz,[3] I. V. Lomonosov,[2,4] and S. A. Piriz[3]

AFFILIATIONS

[1]GSI Helmholtzzentrum für Schwerionenforschung, Planckstraße 1, 64291 Darmstadt, Germany
[2]Institute of Problems of Chemical Physics, Russian Academy of Sciences, Institutskii pr. 18, 142432 Chernogolovka, Russia
[3]E.T.S.I. Industriales, Universidad de Castilla-La Mancha, 13071 Ciudad Real, Spain
[4]Tomsk University, Lenin Ave. 36, 634050 Tomsk, Russia; Lomonosov Moscow State University, GSP-1, Leninskie Gory, 119991 Moscow, Russia; and Moscow Institute of Physics and Technology, Institutskiy Per. 9, 141701 Dolgoprudny, Russia

[a)]Author to whom correspondence should be addressed: n.tahir@gsi.de

ABSTRACT

This paper presents two-dimensional hydrodynamic simulations of implosion of a water sample, which is enclosed in a cylindrical shell of tungsten that is driven by an intense uranium beam. The considered beam parameters match the characteristics of the beam which will be delivered by the heavy ion synchrotron, SIS100, at the Facility for Antiprotons and Ion Research (FAIR). An experimental scheme based on this concept, which is named LAPLAS, is an important part of the high energy density physics research program at FAIR. The simulations show that the LAPLAS implosion leads to a low-entropy compression of water, which generates core conditions of water-rich planets. The importance of this work is underscored by the fact that more than 30% of the discovered extrasolar planets are Neptune-like water-rich planets. To be able to construct a reliable physical model of the formation and evolution of these planets, it is important to have correct understanding of the equation of state of the exotic states of water that exist in the planetary interior. It is thus expected that the knowledge obtained from the LAPLAS experiments will be a very valuable contribution to the field of planetary physics. We show that x-ray radiographic imaging using a high-intensity laser-driven hard x-ray source would be a suitable diagnostic capable of delivering high-resolution images of the hydrodynamic evolution.

I. INTRODUCTION

Up to now, around 4200 confirmed extrasolar planets have been discovered.[1] These include gas giants like Jupiter and Saturn, terrestrial rocky planets, super-Earths with masses up to 10 times Earth mass, and water-rich ice giants like Uranus and Neptune. There are no analogs of super-Earths in our solar system. However, based on the limited amount of data available at present, it is predicted that the super-Earths may span a wide range of possible composition from iron-rich rocky structures to water-rich planets with thick steamy envelope as well as carbon-rich planets. This means that super-Earths could be scaled-up versions of the terrestrial planets or scaled-down versions of ice giants like Neptune that are named mini-Neptunes or lie somewhere in the region between these compositions. The exoplanets span a much broader range of physical conditions compared to the planets in our solar system. This makes the problem of understanding the structure and evolution of these objects more challenging.

Several researchers have proposed theoretical models for the formation and the structure of various types of super-Earths of different masses including solid rocky planets[2–7] as well as water-rich planets named the ocean planets.[4,8–11] An important factor that determines the validity of such models is the accuracy of the equation-of-state (EOS) considered in these models. It is expected that extreme physical conditions are generated in the planetary cores and thus, matter in that region exists in the so-called Warm Dense Matter (WDM) state,[12] which belongs to the High Energy Density (HED) physics regime.[13,14] Development of the EOS of WDM is complicated because it can neither be described using the ordinary condensed matter physics techniques nor by ideal plasma physics methods. It is therefore essential to carry out experiments to measure the EOS properties of these exotic states of matter.

Previously,[15–18] we reported an experiment proposal to generate samples of WDM iron to study the physical conditions in the cores of iron-rich rocky planets. This proposal is named LAPLAS that stands for Laboratory Planetary Sciences, and the experiment design is based on detailed numerical simulations. It has been shown that extreme physical conditions can be induced in a large sample of iron that is imploded in a multi-layered cylindrical target that is driven by an intense heavy ion beam. The beam parameters are assumed to be those of the uranium beam that will be delivered by the heavy ion synchrotron, SIS100, at the Facility for Antiprotons and Ion Research (FAIR),[19,20] at Darmstadt. These simulations have shown that using these beam parameters, a wide range of iron physical parameter space can be accessed that includes the core conditions of Earth and those of super-Earths, up to 10 times more massive than the Earth. It is to be noted that the LAPLAS experiment is one of the important experiments to be done within the framework of HED physics program at FAIR.

Water rich planets are abundant in the universe as over 30% of the discovered exoplanets fall in this category.[1] These include a class of the super-Earths[4,8–11] as well as ice giants like Uranus and Neptune.[21–26] Successful research on these planets requires a very good knowledge of the EOS of different phases of water. For this purpose, we carried out simulation studies of implosion of the LAPLAS target considering water as the sample material. These simulations show that using the FAIR uranium beam, one can generate the extreme physical conditions that cover the core conditions of different types of water rich planets.

In Sec. II, we describe the FAIR accelerator facility, while in Sec. III we discuss the advantages of an intense ion beam driver to produce HED matter. The LAPLAS experimental scheme is described in Sec. IV, whereas the beam and the target parameters used in this study are given in Sec. V. The computer code BIG2 used to do these simulations is described in Sec. VI and the simulation results are presented in Sec. VII. Section VIII deals with the diagnostics, while the conclusions drawn from this work are noted in Sec. IX.

II. FACILITY FOR ANTIPROTONS AND ION RESEARCH: FAIR

FAIR is a heavy-ion accelerator complex exploiting a ring accelerator with a rigidity of 100 Tm (SIS100) capable of accelerating any ion from hydrogen to uranium to relativistic energies above 1 GeV/u with unprecedented intensities of up to 5×10^{11} heavy ions in 70 to 100 ns,[27] whereas the heavy-ion beams with the highest intensities will be reached for low charge state (for example, U28+). The main purpose of this new accelerator is to re-create, in the laboratory, the extreme conditions that could be found in the universe from its creation to the complex nuclear processes taking place during stellar genesis and explosions.[20] To do that, the accelerator will be equipped with high-intensity interaction caves, a nuclear fragment separator, and storage rings targeting rare isotopes[28–30] and antiprotons.[31] An overview of the FAIR accelerator complex is shown in Fig. 1.

When taken collectively, the particles found in the intense heavy-ion pulses can be used to deposit large amounts of energy in excess of 100 kJ/cm^3 over cubic-mm volumes uniformly in a short time to reach high-energy-density states of matter in pressure and temperature. Compared to other methods used to reach HED states with shocks, isochoric heating alleviates the coupling between pressure and temperature found in a shock and enables exploring the full phase-space diagram of equation of states. On the other hand, the high pressure can also be used to produce a multiple-shock reflection scheme to generate planetary core conditions (the LAPLAS experiment). In addition, the strain rates found with such HED driver are lower than those of the more-commonly used laser-driven shocks such that spatially uniform HED states in local thermodynamical equilibrium over cubic-mm samples can be obtained. For this reason, a dedicated target station in the multi-purpose APPA cave[32] is being foreseen, where the LAPLAS setup will be installed.

In the summer of 2018, the civil construction of this new accelerator started in the immediate North of Darmstadt, Germany. Currently, the excavation of the North part of the complex is finished and the underground ring tunnel is under construction. For the southern part of the complex, the civil engineering has been either contracted out or in the final tendering process, such that the construction of the experimental caves and storage rings will begin soon. As of today, a rapid ramping of the facility performance to full specifications is expected in the second half of this decade.

III. ION BEAMS AS TOOL TO GENERATE HIGH ENERGY DENSITY MATTER

High energy density physics spans over wide areas of basic and applied physics, for example, astrophysics, planetary physics, inertial fusion, strongly coupled plasmas, and others. In addition to this, HED physics has great potential for useful industrial applications. Substantial advancements in the technology of high pressure physics during the past decades have made it possible to make significant progress in this important field of research. Static as well as dynamic techniques have been used for this purpose. In the former type of experiments, HED states are induced in the sample at room temperature as it is squeezed in a closed vessel or between anvils. Diamond Anvil Cell (DAC) is a typical example of a static scheme.[33,34] It is also possible to heat the sample with a laser during compression to achieve a higher temperature, for example, see Ref. 35, which reports a temperature of around 3500 K. The time scale of such experiments is from hours to days.

In a dynamic scheme, on the other hand, HED matter is generated by the application of shocks. Shock compression of matter leads

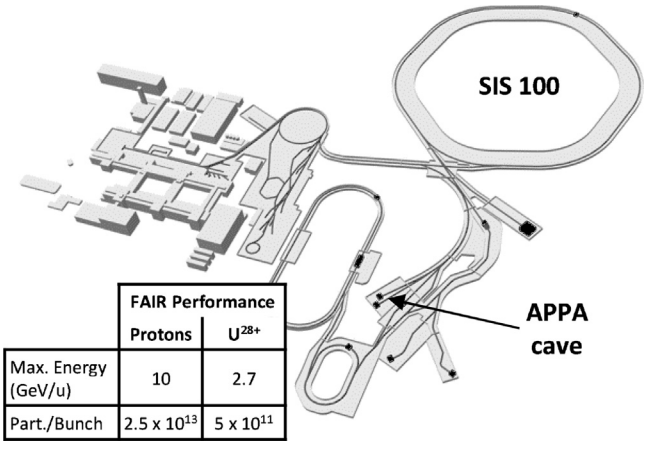

FIG. 1. Overview of the FAIR accelerator complex and expected performance in the APPA cave.

to irreversible heating that generates states of high entropy and high pressure in the sample. Most of the experimental studies on EOS of HED matter have been done using such techniques. The shocks are generated by powerful generators including high power chemical explosives, light gas guns, Z-pinches,[36–39] and powerful lasers.[40–42] Much higher pressures in the Gbar range have been generated using underground nuclear explosions.[43]

Significant technological developments in the field of accelerators have led to the availability of high intensity particle beams. Theoretical studies on beam-matter heating have shown that such beams are an additional, very efficient tool to produce samples of HED matter in the laboratory.[44–61] It is interesting to note that using an ion beam, HED states can be induced in matter using two very different schemes. One scheme is based on isochoric and uniform heating of matter by the beam, while the other employs shock compression of the material. This flexibility is not provided by any other generator. An experiment based on the former scheme named HIHEX (Heavy Ion Heating and Expansion) has been designed with the help of detailed numerical simulations to study the equation-of-state (EOS) properties of HED matter.[53,62–64] The second scheme is employed to propose another experiment (LAPLAS), which uses a multiple shock reflection technique that leads to a low-entropy compression of a sample material that is enclosed in a cylindrical high-Z shell. This multi-layered target is driven by an ion beam that has an annular focal spot. The sample material is imploded to super-solid densities, ultra-high pressures, while the temperature remains relatively low. These are the typical exotic conditions expected to exist in the planetary cores. The details about the beam-target arrangement of the LAPLAS experiment are given in Sec. IV. Previously, we reported simulations of compression of an iron sample which showed that using this method one can produce core conditions of Earth as well as super-Earths of different masses.[15–18] In the present paper, we deal with compression of water to simulate core conditions of water-rich Uranus and Neptune-like planets.

It is to be noted that the HIHEX and the LAPLAS experimental schemes are the major part of the HED physics research program at FAIR, which is named HEDP@FAIR.[65]

It is also worth noting that due to the high efficiency and high repetition rate of the accelerators, heavy ion beams are also considered to be a viable driver for inertial confinement fusion (ICF).[66–76]

IV. LABORATORY PLANETARY SCIENCE: THE LAPALAS EXPERIMENTAL SCHEME

Beam-target geometry of the LAPLAS experiment is shown in Fig. 2. The target is a multi-layered cylinder made of a sample material that is enclosed in a heavy shell of a high-Z material. One face of the target is irradiated with an intense heavy ion beam that has an annular (ring-shaped) focal spot. The annular focal spot can be generated using an rf-wobbler that rotates the beam with very high frequency. Such a system is being designed for this experiment within the framework of the HEDP@FAIR collaboration. Detailed analysis of the energy deposition symmetry issues related to a wobbler has been analyzed and reported in Ref. 78, while the design of a prototype wobbler system has been reported in Ref. 79.

It is to be noted that a hollow beam geometry can be generated by placing a solid cylindrical beam blocker of suitable dimensions upstream the LAPLAS target that will shadow the sample material from direct beam heating. Previously, we simulated such a scheme using a hydrogen sample.[79] This work was related to the study of hydrogen metalization. In these calculations, the achieved final sample temperature was 0.2 eV, which is appropriate for the problem under consideration. However, in the present studies, we are interested in generating planetary core conditions, which require higher temperatures. Therefore, a suitable level of the sample preheat is required that can be easily organized with a wobbler scheme. Moreover, the x-ray radiography diagnostic scheme described in Sec. VIII cannot be used in the presence of a beam blocker. In addition to this, hydrodynamic expansion of the beam blocker may take place during irradiation, which can cause problems. Due to these reasons, a wobbler system is being developed within this project.

It is assumed that the inner radius of the annulus is larger than the radius of the sample material, which is a necessary condition to avoid strong direct heating of the sample by the ion beam (see Fig. 3, which is the cross sectional view of the target shown in Fig. 2). Moreover, it is considered that the outer radius of the focal spot ring is smaller than the outer radius of the surrounding high-Z shell. It is seen in Fig. 3 that a layer of cold material from the high-Z shell, known as "pusher" or "payload," is created between the sample material and the beam-heated region. The payload plays an important role in placing the compression on the desired adiabat. It is also seen that a cold shell around the beam-heated zone remains as a tamper that confines the implosion for a longer time. The target length is assumed to be less than the range of the driver ions so that the energy deposition in the longitudinal direction is uniform. The pressure in the beam heated region increases substantially that launches a shock wave inwards along the radial direction. The shock wave enters the pusher, is subsequently transmitted into the sample, and then reflected at the cylinder axis. The reflected shock moves outwards along the radial direction and is re-reflected at the sample-shell boundary. This process is repeated a few times, while the boundary continues to move inwards, thereby compressing the sample slowly. The optimum sample physical conditions are achieved when the inward motion of the payload is stopped by the high pressure in the compressed sample. This scheme generates a low-entropy compression of the sample material that leads to super-high densities, ultra-high pressures, but relatively low temperatures (typical planetary core conditions).

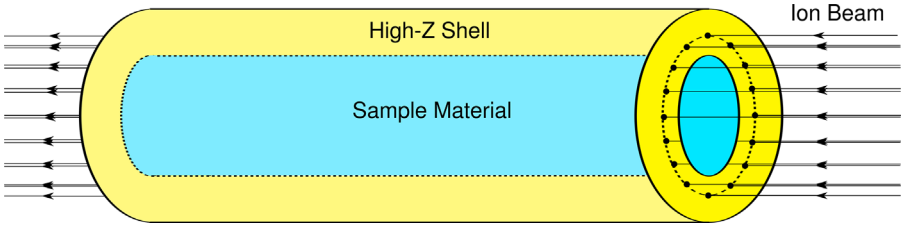

FIG. 2. Beam-target set-up of LAPLAS scheme.

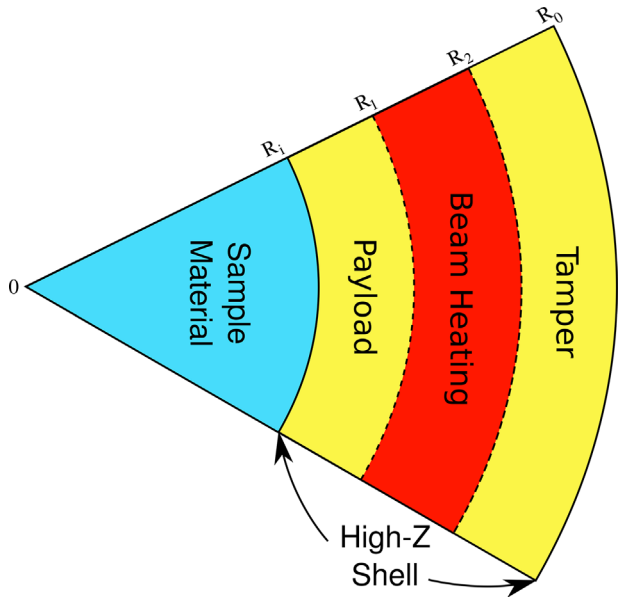

FIG. 3. Cross sectional view of the target shown in Fig. 2.

V. BEAM AND TARGET PARAMETERS USED IN THE STUDY

In the present study, the sample is frozen water (ice), whereas, the surrounding shell is made of tungsten. It is worth noting that the quasi-isentropic implosion of LAPLAS depends on the high density of the payload. On the other hand, the hydrodynamic stability of the imploding payload (see Fig. 3) relies on the mechanical properties of the payload material; the most suitable materials are those with the highest yield strength. Tungsten is one of the materials that better satisfy these two requirements. A recent analysis has shown[80] that the implosion can be sufficiently stable, provided that the symmetry below 2% in the driving pressure is achieved. Such a symmetry level is expected to be achievable with the wobbler system that will rotate the beam with a frequency of 1 GHz.[77]

The cylinder length is 7 mm, while the outer target radius is $R_o = 3$ mm. The target is irradiated with a uranium beam having a particle energy of 1.5 GeV/u. Several beam intensities including, 10^{11}, 2×10^{11}, 3×10^{11}, 4×10^{11}, and 5×10^{11} ions per bunch, respectively, are considered. The bunch length is assumed to be 75 ns. We note that the maximum intensity of the SIS100 uranium beam is expected to be 5×10^{11} ions per bunch, but during the early stages of operation, the intensity may be lower. We therefore have considered different lower intensities in order to explore the possibility of doing research during the initial phases of operation. The focal spot geometry is ring shaped, and the precise parameters are presented in Table I. It is seen in Table I that two values of ice radius, namely, $R_i = 0.2$ mm and 0.3 mm, respectively, are considered. For the former case, two different values of the inner ring radius, $R_1 = 0.3$ mm and 0.4 mm, respectively, are used. This allows a reasonable mass of tungsten payload around the sample material. For the same reason, in the case of $R_i = 0.3$ mm, we use $R_1 = 0.4$ mm and 0.5 mm, respectively. In all the above cases, the width of the ring is assumed to be 1 mm. It is important to note

TABLE I. Target and focal spot parameters.

Case No	R_i (mm)	R_1 (mm)	R_2 (mm)	R_o (mm)
1	0.2	0.4	1.4	3.0
2	0.2	0.3	1.3	3.0
3	0.3	0.5	1.5	3.0
4	0.3	0.4	1.4	3.0

that the transverse intensity distribution in the focal spot is Gaussian. Therefore, due to the wings of the Gaussian distribution, it may be difficult to generate a completely hollow focal spot that will lead to a certain level of energy deposition in the sample as well. For the simplicity of the calculations, we use a spatial power deposition profile as shown in Fig. 4, which is comprised of a constant power step with an amplitude A (which lies in the sample and the payload regions), that is followed by a parabolic power profile. We consider different values of the amplitude, A, varying from 5 to 40% to study the effect of the sample preheat on compression. Moreover, this provides a wide range of physical conditions in water relevant to the planetary core conditions that can be achieved in the LAPLAS experiments.

It is worth noting that as explained in Sec. VIII, the thin wire that becomes source of laser-generated high-energy x-rays, to be used for the radiography of the compressed sample, is placed along the axis upstream the LAPLAS target. If the constant foot power level is too high, the wire will be destroyed by the beam. We believe that the beam spot geometry can be designed in such a manner that the power level at the center of the spot is low enough for the wire to survive. However, this requires further investigations which will be carried out in the future.

VI. COMPUTER CODE BIG

The BIG2 is a two-dimensional hydrodynamic computer code that is based on a Godunov type numerical algorithm, which uses a finite-volume approach in the space-time domain. The fluxes are calculated using the solution of Riemann problem at each inter-cell boundary.[81] It is a conservative scheme that has a second order

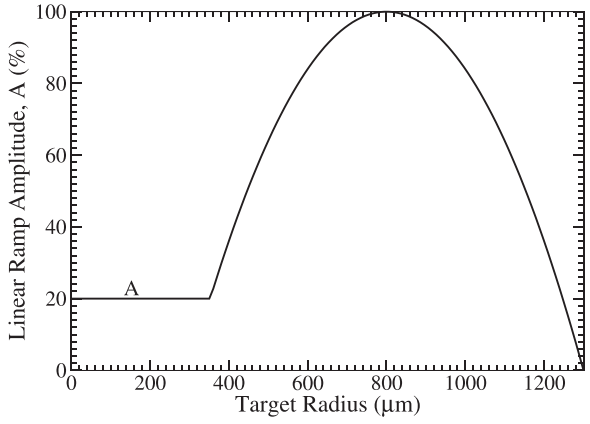

FIG. 4. Spatial power deposition profile.

accuracy in space and first order accuracy in time. The code is based on an Eulerian numerical scheme that uses curvilinear rectangular moving grid. The grid is adaptive to gradient of physical parameters (pressure, temperature, density) due to the condensation of the grid lines. The movement of the grid boundary is calculated in accordance with the type of the boundary, for example, it could be a shock front, a material interface, a free boundary, a rigid wall, and so on. Reconstruction of the grid at the new time step is carried out by quasi-conformal mapping of the rectangular grid to the area with the numerical grid boundary calculated at the new time step, taking into account the gradient of the specified physical parameter. Further details about the numerical techniques used in the code can be found in the reference.[82] The BIG2 code can treat multi-layered targets comprised of different materials and can handle complicated target geometries.

The ion beam energy deposition in the material is calculated assuming a cold stopping model described in Ref. 83. This is a valid approximation because in ion-beam heated targets, the temperature is rather low (below 10 eV) so that the ionization effects are negligible. The plasma effects on the stopping power become important when the ionization level in the material is significant, which requires a much higher temperature.

Due to the beam-heating, the target material passes through different material phases, which are treated using a semi-empirical EOS model described in Refs. 84 and 85. This model considers macroscopically correct equation of state that accounts for solid, liquid, and gaseous states as well as the melting and the evaporating two-phase regions. On our time scales (around 100 ns), we consider the target material is under conditions of the local thermodynamic equilibrium. So we apply in numerical modeling of expanded target the equation of state in tabular form, using Maxwell construction in the two-phase liquid-gas region, as it has been discussed in Ref. 60.

To simulate the mechanical (elastic–plastic) properties of solid materials, we use the non-linear Prandtl–Reuss model with the von Mises yield criterion, which is given by the following differential equations for the deviatoric part S_{ik} of the stress tensor $\sigma_{ik} = -P\,\delta_{ij} + S_{ik}$ (where P is the pressure, and δ_{ik} is the Kronecker tensor):[87]

$$\dot{S}_{ik} = 2GD_{ik}, \tag{1}$$

if $S_{ik}D_{ik} < 0$ or $S_{ik}S_{ik} < \frac{2}{3}Y^2$

$$\dot{S}_{ik} + 2GS_{ik}\frac{S_{mn}D_{mn}}{S_{mn}S_{mn}} = 2GD_{ik}, \tag{2}$$

if $S_{ik}D_{ik} > 0$ and $S_{ik}S_{ik} = \frac{2}{3}Y^2$.

Here G is the shear modulus, Y is the yield strength, and both are parameters characteristic of the solid material, which to the scope of a parametric study are taken as independent and constant parameters. Besides, in Eqs. (1) and (2), D_{ik} is the strain rate tensor

$$D_{ik} = \frac{1}{2}\left(\frac{\partial v_i}{\partial x_k} + \frac{\partial v_k}{\partial x_i} - \frac{2}{3}\frac{\partial v_j}{\partial x_j}\delta_{ik}\right). \tag{3}$$

VII. NUMERICAL SIMULATION RESULTS

The numerical simulation results obtained employing the 2D hydrodynamic computer code, BIG2, are presented in the following. The beam and the target parameters used in this study are given in Sec. V. It is to be noted that a semi-empirical EOS model[84,85] is used for tungsten, while for water, the SESAME data[86] are considered.

A. Beam intensity 5×10^{11}

Here we discuss the results obtained using the highest beam intensity of 5×10^{11} ions per bunch. All the four cases noted in Table I are considered, respectively, as described below.

1. Case 1: $R_i = 0.2$ mm, $R_1 = 0.4$ mm, and $R_2 = 1.4$ mm

These beam and target parameters lead to a sample mass of 1.26×10^{-3} g/cm and a payload mass of 7.24×10^{-2} g/cm. First, we present 2D distributions of the physical conditions generated in the target as a result of beam heating. We note that in this particular case we consider an ideal annular focal spot that is completely hollow. In other words, we assume that the amplitude, A, of the constant power step in Fig. 4, is zero. This is done to study an ideal multiple shock reflection scheme without any interference of preheat.

Figure 5(a) shows the specific energy density distribution in the target at t = 75 ns, the time when the beam has just delivered its total energy. It is seen that a maximum specific energy of about 18 kJ/g is deposited in the tungsten shell.

The corresponding temperature distribution is presented in Fig. 5(b), which shows a maximum temperature of 1.15×10^5 K. This high temperature in the absorption region leads to a high pressure on the order of 3 Mbar [see Fig. 5(c)] that drives the implosion.

The high pressure generates an inmoving as well as an outmoving radial shock, as shown in Fig. 5(d), where we plot the corresponding target density distribution. As explained in Sec. IV, the inmoving shock compresses the tungsten payload to a higher density of around 27 g/cm^3 and is subsequently transmitted into the water region. The shock travels radially toward the cylinder axis, where it is reflected. This shock undergoes multiple reflections between the axis and the water–tungsten boundary, while the heavy payload continuously moves inwards, thereby slowly compressing the water, keeping the entropy level low.

In Fig. 6, we present the density distribution at t = 135 ns, the time of optimum water compression. It is seen that the tungsten payload around water is compressed to a density of about 42 g/cm^3. The water density is around 6.7 g/cm^3, the pressure is on the order of 12.5 Mbar, whereas the average temperature is around 4500 K. These extreme physical conditions are relevant to the interior of water rich planets in our solar system as well as to the exoplanets.

It is also seen from Fig. 6 that the lateral material expansion on the timescale of our interest is not very significant. This implies that the problem is reduced to one-dimensional implosion in the radial direction. We therefore have carried out extensive one-dimensional simulations over the wide range of the beam and target parameters as given in Sec. V. These results are discussed in detailed in the following.

The process of water compression as a result of multiple shock reflection between the axis and the water–tungsten boundary is described in Fig. 7, where we plot the density vs radius at different times during implosion. The vertical lines represent the respective positions of the water–tungsten boundary at different times. The curve corresponding to t = 90 ns shows that the water–tungsten boundary has moved to a radial position of about 154 μm from an initial position of 200 μm, while shock has arrived at point "A" that has a radial

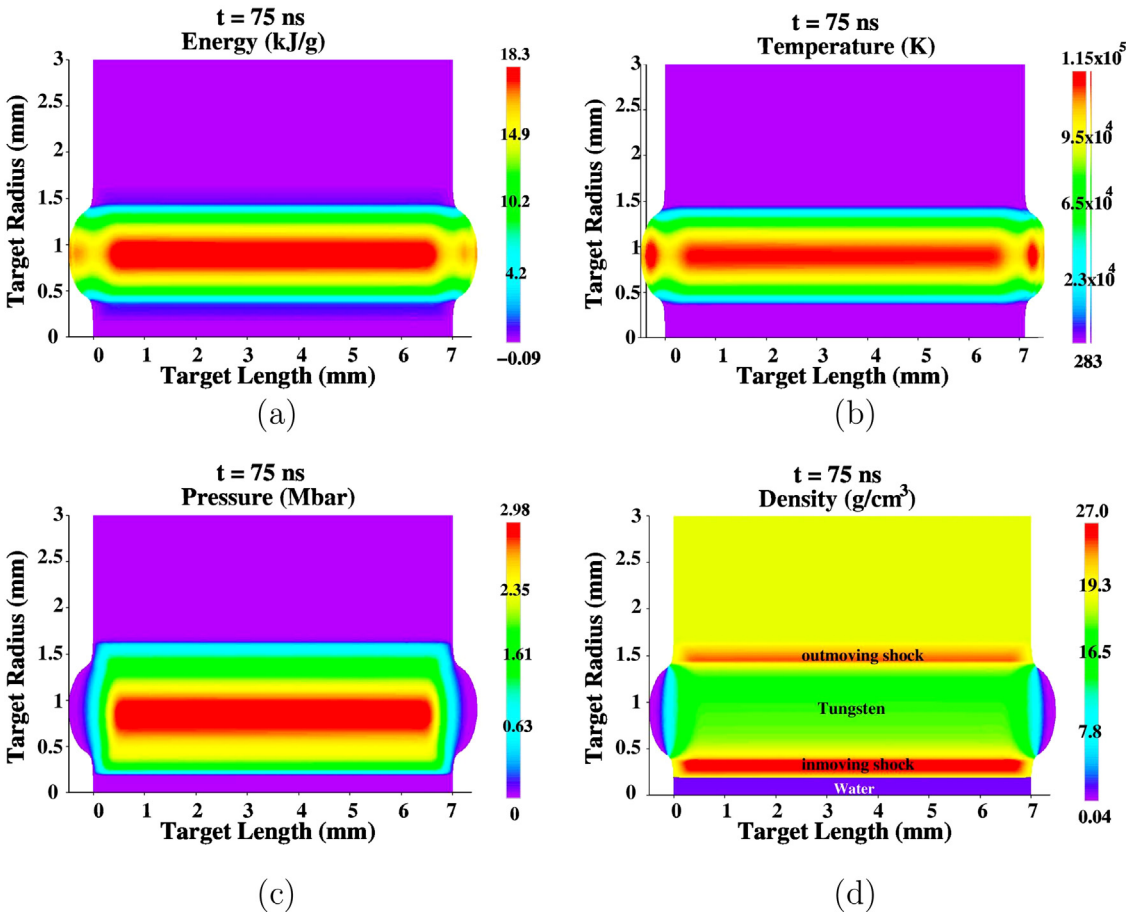

FIG. 5. Target physical conditions generated by BIG2 code at t = 75 ns, intensity = 5×10^{11} uranium ions per bunch, particle energy = 1.5 GeV/u, bunch length = 75 ns, ring shaped focal spot, inner ring radius, $R_1 = 0.4$ mm, outer ring radius, $R_2 = 1.4$ mm, sample radius, $R_i = 0.2$ mm, outer cylinder radius, $R_o = 3$ mm (see Fig. 3); (a) specific energy distribution, (b) temperature distribution, (c) pressure distribution, and (d) density distribution.

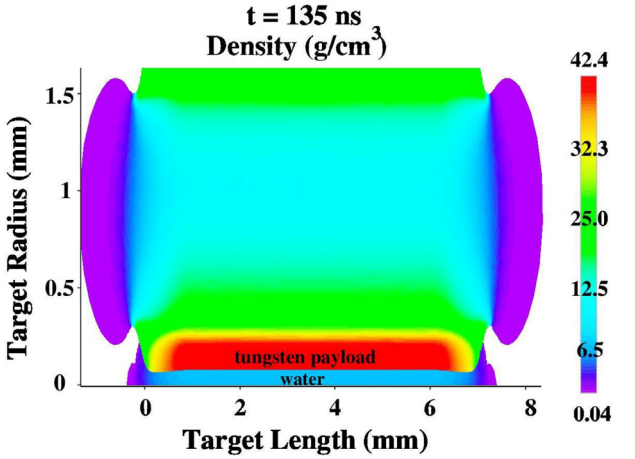

FIG. 6. Same as in Fig. 4(d), but at t = 135 ns.

position of about 95 μm. This shock travels inwards and arrives at the cylinder axis at t = 101 ns (position "B"). The shock is reflected and the front moves outwards (toward the right) and at t = 102 ns it arrives at position "C." The reflected shock is re-reflected at the material interface and the front starts to move toward the left. The shock front is at position "D" at t = 108 ns, which arrives at the axis at t = 112 ns (curve labeled with "E"). This process is repeated a few more times until the optimum compression is achieved at t = 135 ns (curve labeled with "F"). It is interesting to note that the shock becomes weaker every time it is reflected, while the interface boundary continuously moves inwards, thereby slowly compressing the sample material. Such a scheme is known to lead to a low-entropy compression.

Next, we present in Fig. 8, a summary of results obtained from the 1D calculations considering different values of the constant power foot amplitude, A, including 5, 10, 15, 20, 25, 30, 35, and 40%, respectively. In this figure we plot the optimum sample density, temperature and pressure vs the foot amplitude, A. It is seen that as A increases from 5 to 40%, the optimum physical conditions achieved in the sample change significantly. In this range, the maximum temperature increases from 4800 K to 13,500 K, and the pressure varies from

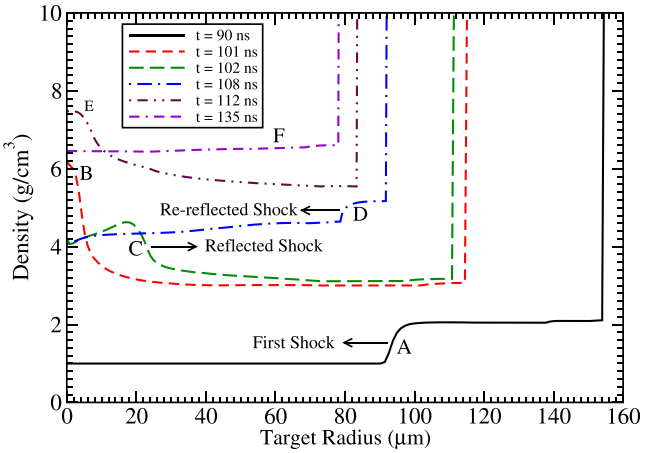

FIG. 7. Density vs radius at different times during implosion: demonstration of multiple shock reflection scheme in the water sample.

11.5 Mbar to 6.2 Mbar, whereas the density decreases from 6.5 g/cm^3 to 4.9 g/cm^3. This suggests that using a suitable value of the amplitude A, one can generate the required set of the physical parameters in the sample.

The precise values of the physical parameters corresponding to the results plotted in Fig. 8, are presented in Table II. It is seen that as the amplitude, A, increases, t_{impl}, the time when the optimum compression is achieved in the sample slightly increases. This is because as A increases, the level of preheat increases that leads to a higher back pressure. This slows down the compression that leads to a longer implosion time, higher temperature, lower density, and lower pressure.

2. Case 2: $R_i = 0.2$ mm, $R_1 = 0.3$ mm, and $R_2 = 1.3$ mm

In this case, the sample mass is the same as in the previous one, while the payload mass has a lower value of 3.01×10^{-2} g/cm. The results are presented in Fig. 9, where we plot profiles of optimum

TABLE II. Optimum physical conditions in compressed water using bunch intensity $= 5 \times 10^{11}$ uranium ions, bunch length = 75 ns, particle energy = 1.5 GeV/u, sample radius, $R_i = 0.2$ mm, annular focal spot with inner ring radius, $R_1 = 0.4$ mm, outer ring radius, $R_2 = 1.4$ mm.

No	A (%)	ρ (g/cm^3)	P (Mbar)	T (K)	t_{impl} (ns)
1	5	6.50	11.5	4.8×10^3	135
2	10	6.05	9.7	6.6×10^3	135
3	15	5.75	8.7	7.9×10^3	136
4	20	5.52	8.03	9×10^3	136
5	25	5.35	7.45	1.04×10^4	136
6	30	5.2	7.0	1.16×10^4	137
7	35	5.1	6.6	1.25×10^4	137
8	40	4.9	6.2	1.35×10^4	137

density, temperature, and pressure in the water sample vs the amplitude, A. It is seen that as A increases from 5 to 40%, significant variation in the values of the physical parameters take place. In this range, the maximum temperature increases from 5200 K to 15,000 K, the pressure varies from 12.1 Mbar to 6.8 Mbar, whereas, the density decreases from 6.6 g/cm^3 to 5 g/cm^3. This again shows that using a suitable value of A, one can achieve a particular set of the physical parameters.

The precise values of the physical parameters achieved in the sample for all the above cases are noted in Table III. It is seen that the implosion time, t_{impl}, increases with an increase in the value of the amplitude, A, for the reasons mentioned above. A comparison between the respective parameters noted in the two tables is interesting. It is seen that in the case of Table II, the implosion time is on the order of 135 ns, whereas in the case of Table III, it is around 115 ns. This difference in the compression time is understandable as in the former case, the payload mass is heavier than in the letter, which makes the implosion process slower.

Also a comparison among the values of the corresponding physical parameters noted in the two tables shows that the results are very similar for the two values of the inner focal spot ring radius,

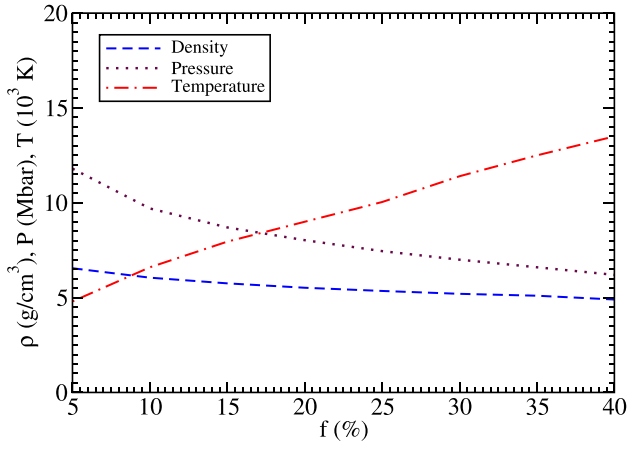

FIG. 8. Average density, temperature, and pressure in compressed water vs foot amplitude for case 1 in Table I, bunch intensity $= 5 \times 10^{11}$.

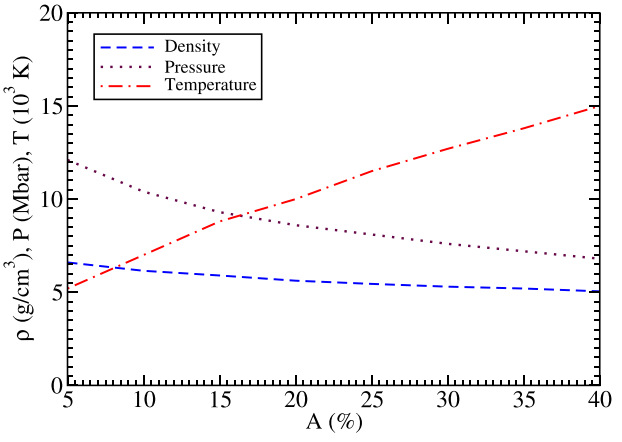

FIG. 9. Average density, temperature, and pressure in compressed water vs foot amplitude for case 2 in Table I, bunch intensity $= 5 \times 10^{11}$.

TABLE III. Optimum physical conditions in compressed water using bunch intensity = 5×10^{11} uranium ions, bunch length = 75 ns, particle energy = 1.5 GeV/u, sample radius, $R_i = 0.2$ mm, annular focal spot with inner ring radius, $R_1 = 0.3$ mm, outer ring radius, $R_2 = 1.3$ mm.

No	A (%)	ρ (g/cm^3)	P (Mbar)	T (K)	t_{impl} (ns)
1	5	6.6	12.1	5.2×10^3	115
2	10	6.15	10.3	7×10^3	116
3	15	5.9	9.3	8.8×10^3	117
4	20	5.62	8.6	10^4	117
5	25	5.45	8.1	1.15×10^4	118
6	30	5.3	7.6	1.25×10^4	118
7	35	5.2	7.2	1.4×10^4	118
8	40	5.05	6.8	1.5×10^4	118

TABLE IV. Optimum physical conditions in compressed water using bunch intensity = 5×10^{11} uranium ions, bunch length = 75 ns, particle energy = 1.5 GeV/u, sample radius, $R_i = 0.3$ mm, annular focal spot with inner ring radius, $R_1 = 0.5$ mm, outer ring radius, $R_2 = 1.5$ mm.

No	A (%)	ρ (g/cm^3)	P (Mbar)	T (K)	t_{impl} (ns)
1	5	6.45	11.4	5.0×10^3	147
2	10	6.08	9.82	6.3×10^3	148
3	15	5.8	8.9	7.8×10^3	149
4	20	5.55	8.2	9×10^3	149
5	25	5.35	7.5	1.02×10^4	150
6	30	5.2	7.1	1.15×10^4	151
7	35	5.05	6.53	1.26×10^4	152
8	40	4.9	6.12	1.35×10^4	152

$R_1 = 0.3$ mm and 0.4 mm, respectively. In the former case, the mass of the tungsten payload around the sample is 3.01×10^{-2} g/cm, whereas, in the latter case, it is around 7.24×10^{-2} g/cm, which is more than a factor of 2 larger. This implies that the results are very much insensitive to substantial variation in the focal spot parameters that leads to significant variation in the payload mass, which demonstrates the stability and robustness of this experimental scheme.

3. Case 3: $R_i = 0.3$ mm, $R_1 = 0.5$ mm, and $R_2 = 1.5$ mm

We now discuss the simulation results achieved using a larger sample radius, $R_i = 0.3$ mm, which leads to a sample mass of 2.83×10^{-3} g/cm, that is more than two times larger than that considered in cases 1 and 2. Also the tungsten payload mass around the sample is 9.65×10^{-2} g/cm. The results obtained in this case are presented in Fig. 10, where we plot profiles of optimum density, temperature, and pressure in the water sample vs the amplitude, A. It is seen that as A increases from 5 to 40%, values of the physical parameters show large variations as the maximum temperature increases from 5000 K to 13,500 K, the pressure varies from 11.4 Mbar to 6.12 Mbar, whereas the density decreases from 6.45 g/cm^3 to 4.9 g/cm^3. This again shows that using a suitable value of A, one can achieve a particular set of the physical parameters.

The exact values of the optimum parameters for the different values of amplitude, A, are presented in Table IV. It is seen that the implosion time, t_{impb} is on the order of 150 ns and its value increases with an increasing value of the amplitude, A. As mentioned above, this is because a larger value of A means more preheat that leads to a higher back pressure, which makes the implosion slower.

4. Case 4: $R_i = 0.3$ mm, $R_1 = 0.4$ mm, and $R_2 = 1.4$ mm

The sample mass in the present case is the same as in case 3, but the payload mass is 2.3 times less than in the previous case and is 4.22×10^{-2} g/cm.

In Fig. 11, we present the optimum water density, temperature, and pressure vs the amplitude, A. It is seen that as A increases from 5 to 40%, the density decreases from 6.6 g/cm^3 to 4.9 g/cm^3, whereas the temperature increases from 5900 K to 15000 K due the increase in the preheat level. The overall effect on the pressure is that it is reduced from 12.15 Mbar to 6.5 Mbar.

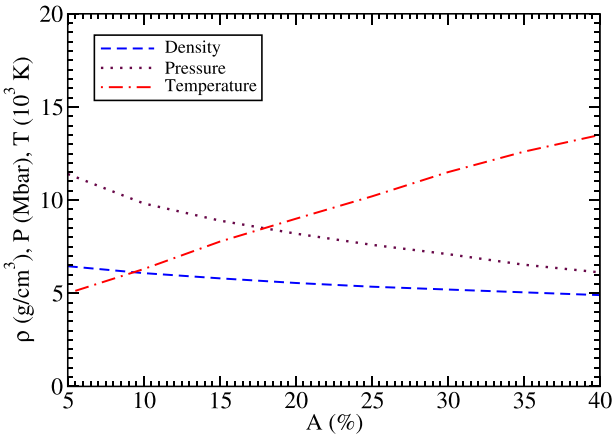

FIG. 10. Average density, temperature, and pressure in compressed water vs foot amplitude for case 3 in Table I, bunch intensity = 5×10^{11}.

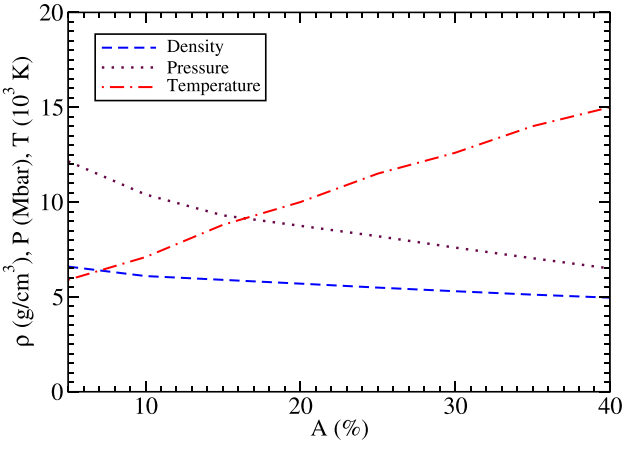

FIG. 11. Average density, temperature, and pressure in compressed water vs foot amplitude for case 4 in Table I, bunch intensity = 5×10^{11}.

TABLE V. Optimum physical conditions in compressed water using bunch intensity = 5×10^{11} uranium ions, bunch length = 75 ns, particle energy = 1.5 GeV/u, sample radius, $R_i = 0.3$ mm, annular focal spot with inner ring radius, $R_1 = 0.4$ mm, outer ring radius, $R_2 = 1.4$ mm.

No	A (%)	ρ (g/cm^3)	P (Mbar)	T (K)	t_{impl} (ns)
1	5	6.6	12.15	5.9×10^3	135
2	10	6.1	10.4	6.9×10^3	136
3	15	5.9	9.3	8.8×10^3	136
4	20	5.7	8.75	10^4	137
5	25	5.5	8.2	1.15×10^4	137
6	30	5.3	7.6	1.26×10^4	138
7	35	5.12	7.04	1.4×10^4	139
8	40	4.96	6.5	1.5×10^4	139

TABLE VI. Optimum physical conditions in compressed water using bunch intensity = 4×10^{11} uranium ions, bunch length = 75 ns, particle energy = 1.5 GeV/u, sample radius, $R_i = 0.2$ mm, annular focal spot with inner ring radius, $R_1 = 0.4$ mm, outer ring radius, $R_2 = 1.4$ mm.

No	A (%)	ρ (g/cm^3)	P (Mbar)	T (K)	t_{impl} (ns)
1	5	6.1	9.51	4.38×10^3	137
2	10	5.68	8.2	5.34×10^3	137
3	15	5.4	7.3	6.53×10^3	138
4	20	5.2	6.7	7.52×10^3	138
5	25	5.1	6.3	8.66×10^3	139
6	30	4.9	5.85	9.51×10^3	139
7	35	4.8	5.53	1.01×10^4	140
8	40	4.65	5.3	1.07×10^4	140

The precise values of the optimum parameters for the different cases are presented in Table V. It is seen that in this case the implosion time is around 135 ns, which is shorter than in Table IV, because of the difference in the payload mass in the two cases.

It is important to note that in this study, the sample as well as the payload mass is varied by more than a factor of 2, respectively. The above analysis shows that the results are insensitive to such significant changes in the input parameters, which is a very good indicator for the success of the LAPLAS experimental scheme.

B. Beam intensity 4×10^{11}

In the following, we present the numerical simulation results using an intensity of 4×10^{11} ions per bunch considering four different sets of beam and target parameters noted in Table I.

1. Case 1: $R_i = 0.2$ mm, $R_1 = 0.4$ mm, and $R_2 = 1.4$ mm

The results corresponding to this case are summarized in Fig. 12, where we plot the optimum sample density, temperature, and pressure vs the constant power step amplitude, A. It is seen that as A increases from 5% to 40%, the density changes from 6 g/cm^3 to 4.6 g/cm^3, while the temperature increases from 4300 K to 10,500 K. The pressure also varies from 9.5 Mbar to about 5 Mbar. Precise values of the parameters are noted in Table VI. It is seen that the implosion time, T_{impb} increases with A.

2. Case 2: $R_i = 0.2$ mm, $R_1 = 0.3$ mm, and $R_2 = 1.3$ mm

A summary of the results obtained using this set of parameters is presented in Fig. 13, which shows the density, temperature, and pressure profiles in the water region vs the constant power step amplitude, A, under the optimum conditions. It is seen that over the considered range of A, the density decreases from 6.2 g/cm^3 to 4.8 g/cm^3, whereas the temperature increases from 4300 K to 10700 K. Also the pressure decreases from 10 Mbar to about 5.8 Mbar. The precise values of the parameters are given in Table VII. It is seen that the implosion time is on the order of 120 ns.

3. Case 3: $R_i = 0.3$ mm, $R_1 = 0.5$ mm, and $R_2 = 1.5$ mm

Figure 14 presents a summary of the results obtained using this set of input parameters. It shows the density, temperature, and pressure

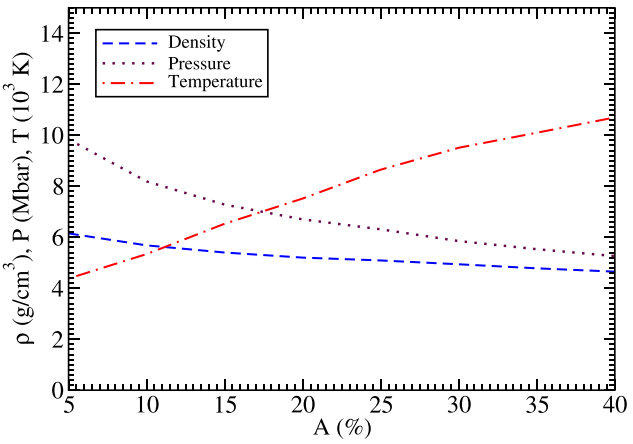

FIG. 12. Average density, temperature, and pressure in compressed water vs foot amplitude for case 1 in Table I, bunch intensity = 4×10^{11}.

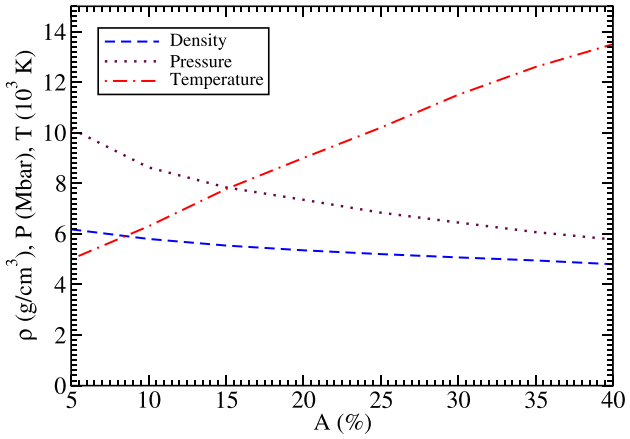

FIG. 13. Average density, temperature, and pressure in compressed water vs foot amplitude for case 2 in Table I, bunch intensity = 4×10^{11}.

TABLE VII. Optimum physical conditions in compressed water using bunch intensity = 4×10^{11} uranium ions, bunch length = 75 ns, particle energy = 1.5 GeV/u, sample radius, $R_i = 0.2$ mm, annular focal spot with inner ring radius, $R_1 = 0.3$ mm, outer ring radius, $R_2 = 1.3$ mm.

No	A (%)	ρ (g/cm^3)	P (Mbar)	T (K)	t_{impl} (ns)
1	5	6.2	10.2	4.38×10^3	118
2	10	5.8	8.6	5.34×10^3	119
3	15	5.54	7.8	6.53×10^3	120
4	20	5.35	7.35	7.52×10^3	121
5	25	5.2	6.84	8.66×10^3	121
6	30	5.0	6.45	9.51×10^3	122
7	35	4.95	6.1	1.01×10^4	122
8	40	4.8	5.8	1.07×10^4	122

TABLE VIII. Optimum physical conditions in compressed water using bunch intensity = 4×10^{11} uranium ions, bunch length = 75 ns, particle energy = 1.5 GeV/u, sample radius, $R_i = 0.3$ mm, annular focal spot with inner ring radius, $R_1 = 0.5$ mm, outer ring radius, $R_2 = 1.5$ mm.

No	A (%)	ρ (g/cm^3)	P (Mbar)	T (K)	t_{impl} (ns)
1	5	6.0	9.3	4.56×10^3	151
2	10	5.6	8.0	5.1×10^3	152
3	15	5.4	7.2	6.25×10^3	153
4	20	5.2	6.5	7.44×10^3	154
5	25	5.0	6.2	8.58×10^3	155
6	30	4.9	5.8	9.76×10^3	155
7	35	4.7	5.4	1.03×10^4	156
8	40	4.6	5.2	1.06×10^4	156

vs the constant power step amplitude, A, in water under optimum conditions. It is seen that over the considered range, the density decreases from 6 g/cm^3 to 4.6 g/cm^3, the temperature increases from 4500 K to 10,600 K, and the pressure also decreases from 9.3 Mbar to 5.2 Mbar.

The precise values of the parameters are presented in Table VIII, which shows that the implosion time is around 155 ns.

4. Case 4: $R_i = 0.3$ mm, $R_1 = 0.4$ mm, and $R_2 = 1.4$ mm

A summary of the results corresponding to this case is presented in Fig. 15, where we plot the optimum water physical conditions vs the constant power step amplitude, A. It is seen that over the considered range of A, the density changes from 6.1 g/cm^3 to 4.6 g/cm^3, the temperature increases from about 4800 K to 10,700 K and the pressure varies from 9.8 Mbar to 5.2 Mbar. The precise values of the parameters are noted in Table IX which shows that t_{impl} is about 144 ns.

C. Beam intensity 3×10^{11}

In this section, we present the simulation results obtained assuming an intensity of 3×10^{11} ions/bunch. Although we have carried out simulations considering all the four sets of beam and target parameters noted in Table I, we only present results for the cases 1 and 2 to avoid repetition. This means that we only present results corresponding to a sample radius of 0.2 mm, using inner ring radius of 0.4 mm and 0.3 mm, respectively.

1. Case 1: $R_i = 0.2$ mm, $R_1 = 0.4$ mm, and $R_2 = 1.4$ mm

In Fig. 16, a summary of the simulation results obtained using this set of the beam and target parameters is presented. Here again we plot the optimum density, temperature, and pressure vs the constant power step amplitude parameter, A. It is seen that as parameter A varies between 5% to 40%, the density decreases from 5.5 g/cm^3 to 4.4 g/cm^3, whereas the temperature increases from about 3600 K to 8300 K. The pressure changes from about 7.25 Mbar to 4.2 Mbar. The precise values of these parameters are noted in Table X. It is seen that t_{impl} is on the order of 148 ns.

2. Case 2: $R_i = 0.2$ mm, $R_1 = 0.3$ mm, and $R_2 = 1.3$ mm

Figure 17 shows the optimum water density, temperature, and the pressure vs the constant power step amplitude A. It is seen that

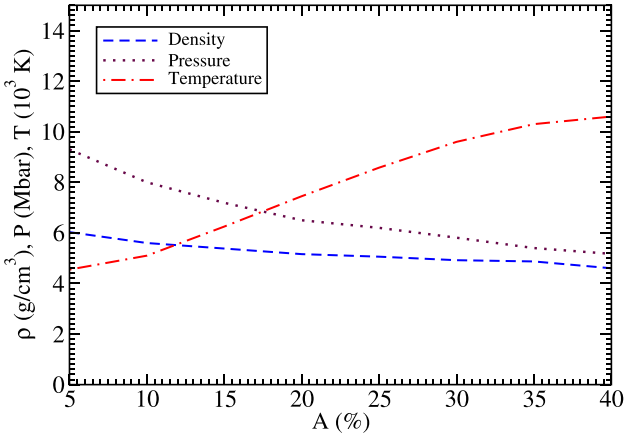

FIG. 14. Average density, temperature, and pressure in compressed water vs foot amplitude for case 3 in Table I, bunch intensity = 4×10^{11}.

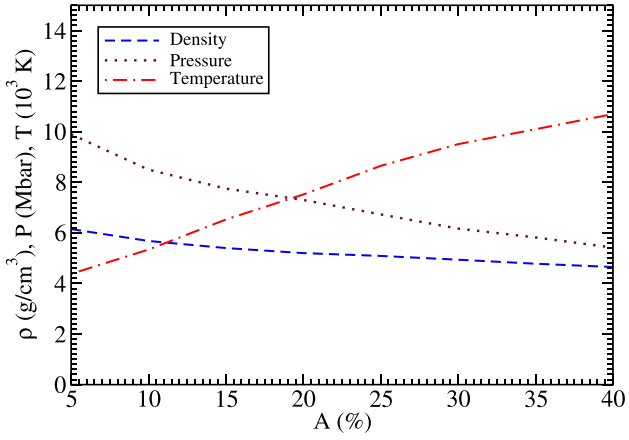

FIG. 15. Average density, temperature, and pressure in compressed water vs foot amplitude for case 4 in Table I, bunch intensity = 4×10^{11}.

TABLE IX. Optimum physical conditions in compressed water using bunch intensity = 4×10^{11} uranium ions, bunch length = 75 ns, particle energy = 1.5 GeV/u, sample radius, $R_i = 0.3$ mm, annular focal spot with inner ring radius, $R_1 = 0.4$ mm, outer ring radius, $R_2 = 1.4$ mm.

No	A (%)	ρ (g/cm^3)	P (Mbar)	T (K)	t_{impl} (ns)
1	5	6.15	9.84	4.81×10^3	142
2	10	5.7	8.2	5.34×10^3	143
3	15	5.4	7.28	6.53×10^3	144
4	20	5.2	6.7	7.52×10^3	144
5	25	5.1	6.34	8.66×10^3	145
6	30	4.9	5.85	9.51×10^3	145
7	35	4.8	5.52	1.01×10^4	146
8	40	4.65	5.26	1.07×10^4	146

over the considered range of the parameter, A, the density decreases from a value of 5.7 g/cm^3 to 4.48 g/cm^3, and the temperature increases from 4100 K to 9400 K, while the pressure decreases from 8 Mbar to about 4.7 Mbar. The precise values of the parameters are noted in Table XI which shows that t_{impl} in this case is about 125 ns. A comparison between Tables X and XI shows that the corresponding parameter values are quite similar, which again indicates the stability of the LAPLAS experimental scheme even for this moderate intensity. It is also to be noted that the results obtained using the larger sample mass corresponding to $R_i = 0.3$ mm, show a similar pattern.

D. Beam intensity 2×10^{11}

In the following, we present the simulation results obtained considering a lower intensity of 2×10^{11} ions/bunch. Again we limit the discussion to the results obtained using the cases 1 and 2 mentioned in Table I.

1. Case 1: $R_i = 0.2$ mm, $R_1 = 0.4$ mm, and $R_2 = 1.4$ mm

The simulation results obtained using the considered set of the input parameters are shown in Fig. 18, where we plot the optimum

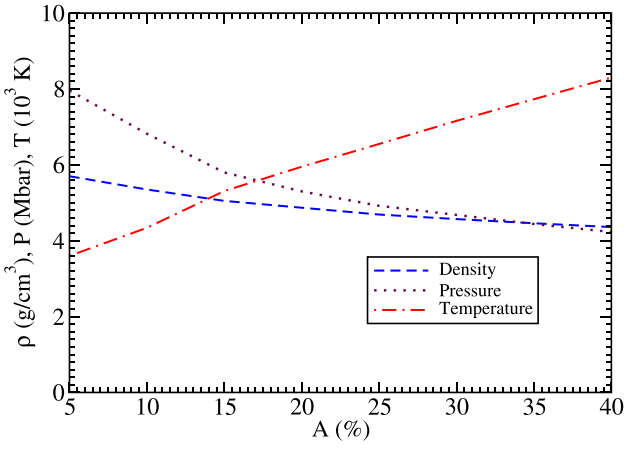

FIG. 16. Average density, temperature and pressure in compressed water vs foot amplitude for case 1 in Table I, bunch intensity = 3×10^{11}.

TABLE X. Optimum physical conditions in compressed water using bunch intensity = 3×10^{11} uranium ions, bunch length = 75 ns, particle energy = 1.5 GeV/u, sample radius, $R_i = 0.2$ mm, annular focal spot with inner ring radius, $R_1 = 0.4$ mm, outer ring radius, $R_2 = 1.4$ mm.

No	A (%)	ρ (g/cm^3)	P (Mbar)	T (K)	t_{impl} (ns)
1	5	5.5	7.25	3.59×10^3	147
2	10	5.35	6.45	4.34×10^3	147
3	15	5.05	5.5	5.31×10^3	148
4	20	4.87	5.3	5.95×10^3	148
5	25	4.68	4.92	6.55×10^3	149
6	30	4.57	4.68	7.61×10^3	149
7	35	4.46	4.44	7.73×10^3	149
8	40	4.36	4.23	8.3×10^3	149

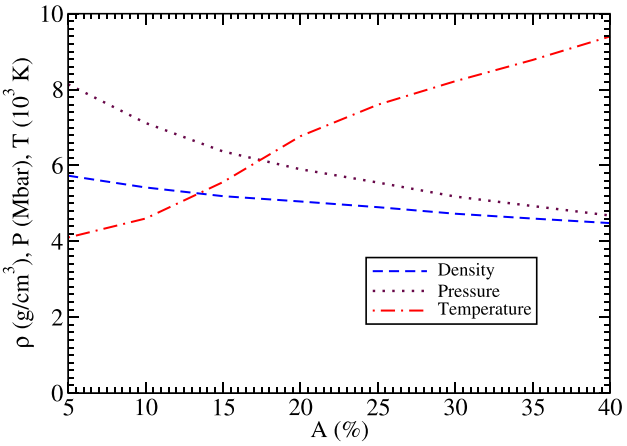

FIG. 17. Average density, temperature, and pressure in compressed water vs foot amplitude for case 2 in Table I, bunch intensity = 3×10^{11}.

sample density, temperature, and pressure vs the constant power step amplitude, A. This figure shows that as the value of the parameter A increases from 5% and 40%, the density decreases from about 5 g/cm^3 to 4 g/cm^3, while the temperature increases from around 3000 to

TABLE XI. Optimum physical conditions in compressed water using bunch intensity = 3×10^{11} uranium ions, bunch length = 75 ns, particle energy = 1.5 GeV/u, sample radius, $R_i = 0.2$ mm, annular focal spot with inner ring radius, $R_1 = 0.3$ mm, outer ring radius, $R_2 = 1.3$ mm.

No	A (%)	ρ (g/cm^3)	P (Mbar)	T (K)	t_{impl} (ns)
1	5	5.7	8.0	4.15×10^3	124
2	10	5.42	7.12	4.46×10^3	124
3	15	5.19	6.2	5.56×10^3	125
4	20	5.05	5.9	6.83×10^3	125
5	25	4.9	5.55	7.66×10^3	126
6	30	4.72	5.18	8.11×10^3	126
7	35	4.6	4.93	8.78×10^3	126
8	40	4.48	4.7	9.4×10^3	126

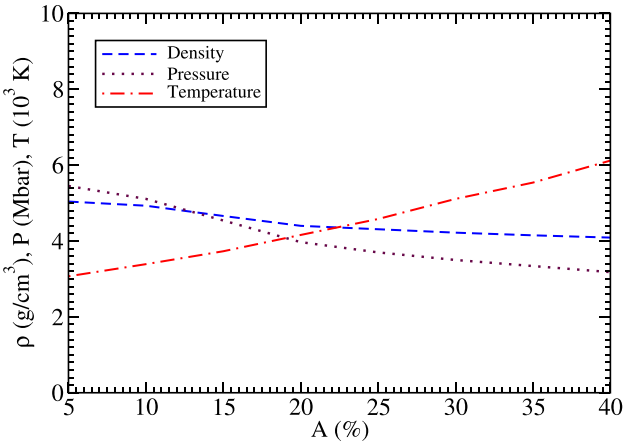

FIG. 18. Average density, temperature, and pressure in compressed water vs foot amplitude for case 1 in Table I, bunch intensity = 2×10^{11}.

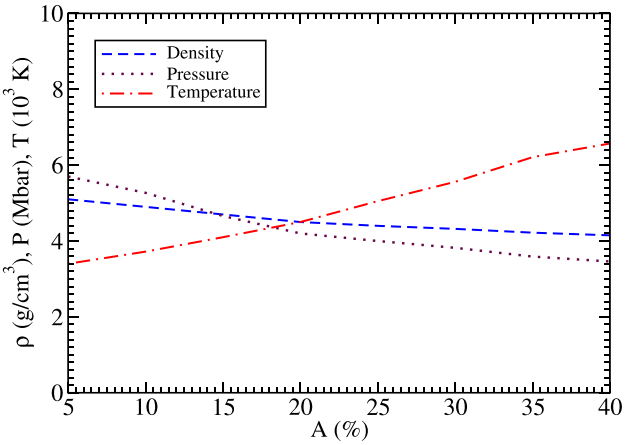

FIG. 19. Average density, temperature, and pressure in compressed water vs foot amplitude for case 2 in Table I, bunch intensity = 2×10^{11}.

6000 K. Also the pressure decreases from about 5.5 Mbar to around 3 Mbar. The precise values of these parameters are noted in Table XII. It is seen that in this set of calculations, t_{impl} is around 154 ns.

2. Case 2: $R_i = 0.2$ mm, $R_1 = 0.3$ mm, and $R_2 = 1.3$ mm

We now discuss the simulation results corresponding to the above set of the beam and the target parameters. In Fig. 19, we plot the optimum sample density, pressure, and temperature vs the constant power step amplitude, A. It is seen that over the considered range of the parameter, A, the density decreases from about 5 g/cm^3 to 4 g/cm^3, the temperature increases from 3400 K to 6500 K, and the pressure is reduced from 5.7 Mbar to 3.4 Mbar. One can, therefore, generate any required set of the physical parameters by choosing an appropriate value of the parameter A. The exact values of the physical parameters are noted in Table XIII, showing an implosion time of the order of 127 ns.

E. Beam intensity 10^{11}

Finally, we discuss the simulation results using the lowest considered bunch intensity of 10^{11}. We only present results obtained using the input parameter sets corresponding to cases 1 and 2. This means a sample radius of 0.2 mm and an inner ring radius of 0.3 mm and 0.4 mm, respectively.

1. Case 1: $R_i = 0.2$ mm, $R_1 = 0.4$ mm, and $R_2 = 1.4$ mm

The results obtained using this set of input parameters are presented in Fig. 20, where we plot the optimum water density, temperature, and pressure vs the constant power step amplitude, A.

It is seen that over the considered range of the parameter A, the density decreases from about 4.3 g/cm^3 to 3.8 g/cm^3, while the temperature increases from 1700 K to 3600 K. Also the pressure changes from 3.55 Mbar to 2.3 Mbar. The exact values of the physical parameters are noted in Table XIV, which shows an implosion time of about 165 ns.

2. Case 2: $R_i = 0.2$ mm, $R_1 = 0.3$ mm, and $R_2 = 1.3$ mm

Figure 21 presents the results achieved using this particular set of the beam and target parameters. In this figure, we plot the density, temperature, and pressure vs constant power step amplitude, A, over a range of 5% to 40%. It is seen that the density decreases from 4.4 g/cm^3

TABLE XII. Optimum physical conditions in compressed water using bunch intensity = 2×10^{11} uranium ions, bunch length = 75 ns, particle energy = 1.5 GeV/u, sample radius, $R_i = 0.2$ mm, annular focal spot with inner ring radius, $R_1 = 0.4$ mm, outer ring radius, $R_2 = 1.4$ mm.

No	A (%)	ρ (g/cm^3)	P (Mbar)	T (K)	t_{impl} (ns)
1	5	5.04	5.45	3.07×10^3	153
2	10	4.93	5.11	3.39×10^3	153
3	15	4.66	4.54	3.73×10^3	154
4	20	4.4	3.92	4.16×10^3	154
5	25	4.31	3.7	4.58×10^3	155
6	30	4.22	3.5	5.11×10^3	156
7	35	4.15	3.34	5.54×10^3	156
8	40	4.1	3.18	6.12×10^3	156

TABLE XIII. Optimum physical conditions in compressed water using bunch intensity = 2×10^{11} uranium ions, bunch length = 75 ns, particle energy = 1.5 GeV/u, sample radius, $R_i = 0.2$ mm, annular focal spot with inner ring radius, $R_1 = 0.3$ mm, outer ring radius, $R_2 = 1.3$ mm.

No	A (%)	ρ (g/cm^3)	P (Mbar)	T (K)	t_{impl} (ns)
1	5	5.1	5.7	3.4×10^3	126
2	10	4.9	5.27	3.72×10^3	126
3	15	4.7	4.7	4.1×10^3	127
4	20	4.6	4.4	4.5×10^3	128
5	25	4.5	4.2	5.05×10^3	128
6	30	4.32	3.82	5.56×10^3	129
7	35	4.22	3.59	6.17×10^3	129
8	40	4.15	3.46	6.57×10^3	129

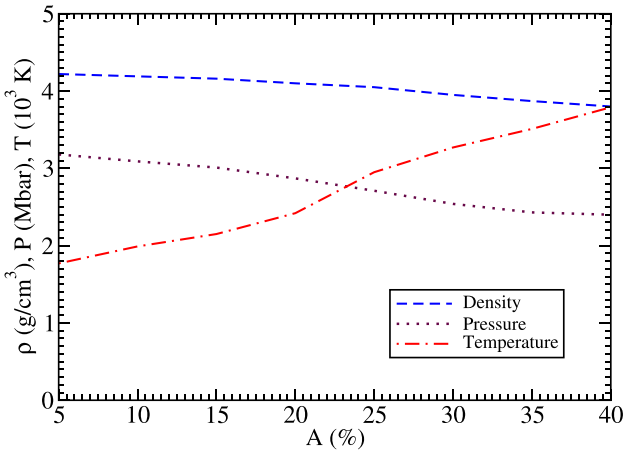

FIG. 20. Average density, temperature, and pressure in compressed water vs foot amplitude for case 1 in Table I, bunch intensity = 10^{11}.

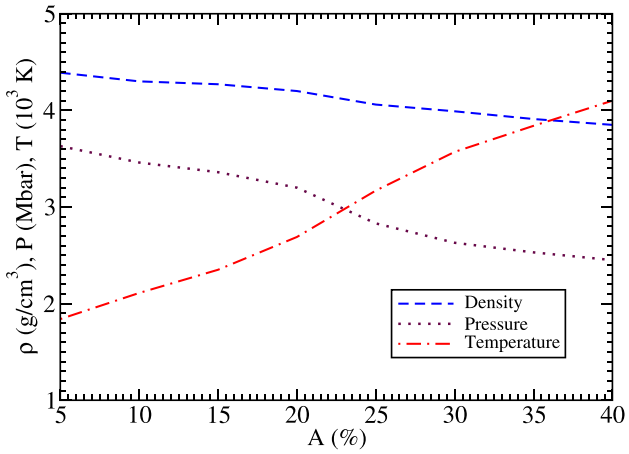

FIG. 21. Average density, temperature, and pressure in compressed water vs foot amplitude for case 2 in Table I, bunch intensity = 10^{11}.

to 3.9 g/cm^3, whereas the temperature increases from 1800 K to 4000 K. The pressure decreases from 3.5 Mbar to 2.6 Mbar. Detailed values of the achieved parameters are noted in Table XV. It is seen that t_{impl} is around 148 ns.

A comparison between Tables XIV and XV shows that the results are insensitive to variation in the inner ring radius which leads to a variation in the payload mass by more than a factor of 2. Similar behavior is observed for the cases 3 and 4 in Table I. This suggests the stability of the LAPLAS scheme even for this relatively low intensity. It is also interesting to note that the values of the implosion time, t_{impl}, presented in Tables II–XV increase as the beam intensity changes from 5×10^{11} to 10^{11} ions per bunch. This is because the driving pressure decreases as the bunch intensity is reduced that makes the implosion process slower and less efficient.

F. Overall discussion of results

In Figs. 22(a)–22(d), we plot the optimum water density, temperature, and pressure vs the bunch intensity using different values of the constant power step amplitude, A, including 5%, 10%, 15%, and 20%, respectively. These results correspond to the case using the sample radius, $R_i = 0.2$ mm, inner ring radius, $R_1 = 0.4$ mm, and outer ring radius, $R_2 = 1.4$ mm.

Figure 22(a) shows that assuming A = 5%, using the highest bunch intensity of 5×10^{11}, the achieved density, temperature and pressure are 6.55 g/cm^3, 4800 K, and 11.8 Mbar, respectively. For the lowest bunch intensity of 10^{11}, the corresponding values are 4.36 g/cm^3, 1700 K, and 3.55 Mbar, respectively. Any required parameter sets within this range can be obtained by choosing a suitable value of the parameter, A.

Figure 22(b) presents results obtained assuming A = 10%. In this case, the limiting values of density, temperature, and pressure are 6.15 g/cm^3 and 4.3 g/cm^3, 7000 and 2110 K, and 10.3 Mbar and 3.46 Mbar, respectively.

Figure 22(c) shows results considering A = 15%. In this case, the achieved density range is 5.9 g/cm^3 to 4.7 g/cm^3, the temperature range is 8800 K to 2350 K and the corresponding pressure range is 9.3 Mbar to 3.36 Mbar for the highest and the lowest bunch intensity, respectively.

Figure 22(d) presents results obtained assuming A = 20%. In this case, the limiting values of density, temperature, and pressure are

TABLE XIV. Optimum physical conditions in compressed water using bunch intensity = 10^{11} uranium ions, bunch length = 75 ns, particle energy = 1.5 GeV/u, sample radius, $R_i = 0.2$ mm, annular focal spot with inner ring radius, $R_1 = 0.4$ mm, outer ring radius, $R_2 = 1.4$ mm.

No	A (%)	ρ (g/cm^3)	P (Mbar)	T (K)	t_{impl} (ns)
1	5	4.36	3.55	1.7×10^3	165
2	10	4.3	3.44	1.93×10^3	165
3	15	4.27	3.34	2.21×10^3	165
4	20	4.18	3.13	2.61×10^3	165
5	25	4.04	2.74	2.97×10^3	166
6	30	3.92	2.5	3.24×10^3	166
7	35	3.82	2.33	3.92×10^3	166
8	40	3.77	2.16	3.64×10^3	166

TABLE XV. Optimum physical conditions in compressed water using bunch intensity = 10^{11} uranium ions, bunch length = 75 ns, particle energy = 1.5 GeV/u, sample radius, $R_i = 0.2$ mm, annular focal spot with inner ring radius, $R_1 = 0.3$ mm, outer ring radius, $R_2 = 1.3$ mm.

No	A (%)	ρ (g/cm^3)	P (Mbar)	T (K)	t_{impl} (ns)
1	5	4.39	3.63	1.84×10^3	147
2	10	4.3	3.46	2.11×10^3	147
3	15	4.29	3.36	2.35×10^3	148
4	20	4.2	3.2	2.69×10^3	148
5	25	4.06	2.83	3.17×10^3	149
6	30	3.99	2.64	3.57×10^3	149
7	35	3.91	2.53	3.94×10^3	129
8	40	3.85	2.45	4.1×10^3	149

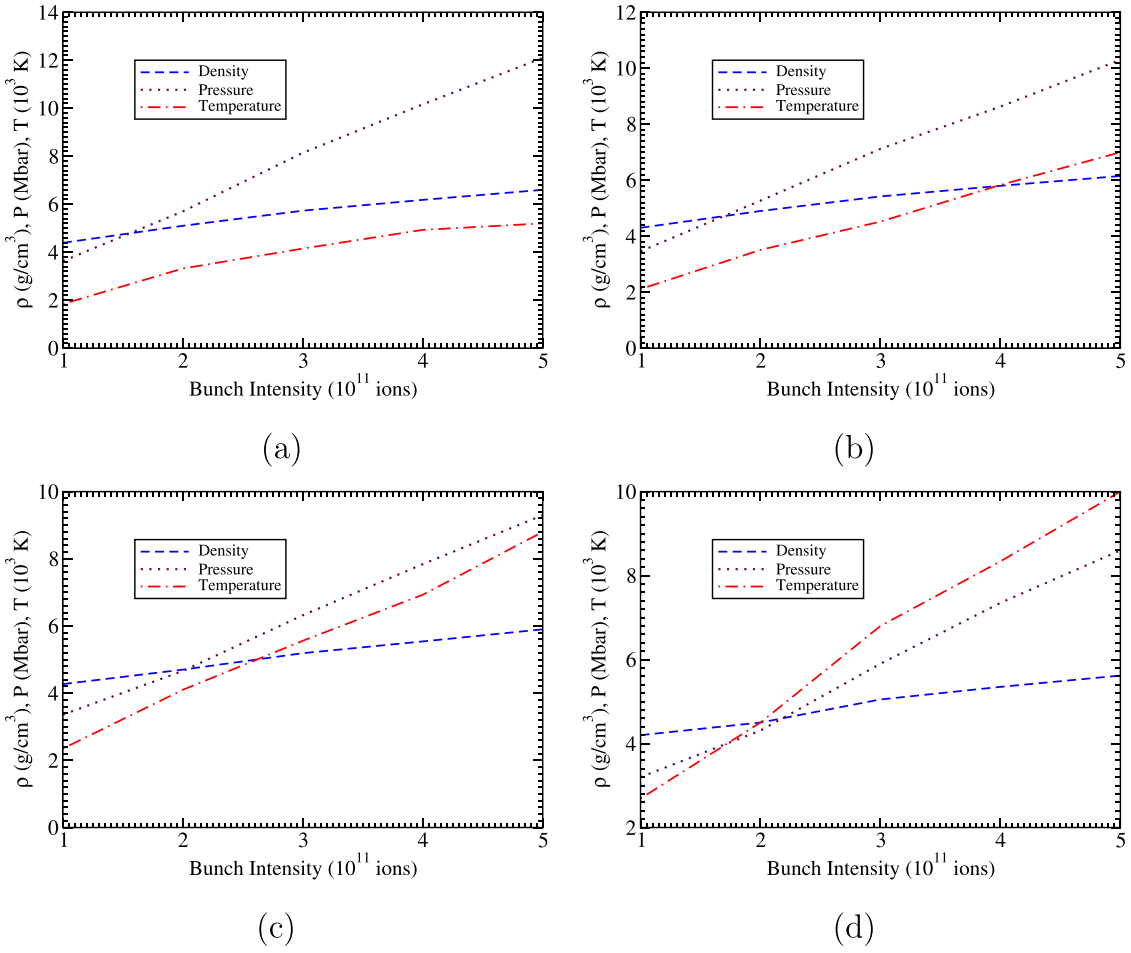

FIG. 22. Density, ρ, temperature, T, and pressure, P vs bunch intensity, particle energy = 1.5 GeV/u, bunch length = 75 ns, sample radius, R_i = 0.2 mm, inner ring radius, R_1 = 0.4 mm, outer ring radius, R_2 = 1.4 mm; constant power step amplitude, A: (a) 5%, (b) 10%, (c) 15%, and (d) 20%.

5.6 g/cm^3 and 4.2 g/cm^3, 7000 K to 3170 K, and 8.6 Mbar and 3.2 Mbar, respectively.

In Fig. 23, we plot the same parameters as in Fig. 22, but using A = 25, 30, 35, and 40%, respectively.

Figure 23(a) shows that using A = 25%, the water density, temperature, and pressure corresponding to the highest bunch intensity are 5.45 g/cm^3, 11,500 K, and 8.1 Mbar, respectively. Using the minimum bunch intensity, on the other hand, the corresponding values of these parameters are 4 g/cm^3, 3170 K, and 2.8 Mbar, respectively.

Figure 23(b) presents results obtained assuming A = 30%. The maximum values of the density, temperature and pressure are 5.3 g/cm^3, 12,500 K, and 7.6 Mbar, respectively, whereas the minimum values of these parameters are 4 g/cm^3, 3570 K, and 2.6 Mbar, respectively.

Figure 23(c) shows the water physical parameters using A = 35%. It is seen that the density, temperature, and pressure corresponding to the highest bunch intensity are 5.2 g/cm^3, 14000 K, and 7.2 Mbar, respectively. Using the minimum bunch intensity, on the other hand, the corresponding values of these parameters are 3.9 g/cm^3, 3840 K, and 2.5 Mbar, respectively.

Figure 23(d) shows results assuming A = 40%. In this case, the achieved density range is 5 g/cm^3 to 3.8 g/cm^3, the temperature range is 15,000 K to 4100 K, and the corresponding pressure range is 6.8 Mbar to 2.45 Mbar corresponding to the highest and the lowest bunch intensity, respectively.

The above discussion shows that a very wide range of extreme physical conditions that are expected to exist in the core of the water rich planets can be generated by compressing a reasonable mass of the water sample in the LAPLAS scheme. Any required set of the physical parameters can be obtained by using a suitable value of the bunch intensity and the constant power step amplitude, A.

VIII. DIAGNOSTICS

Diagnosing the short-lived WDM samples generated in laboratory experiments is a formidable challenge in itself. Due to the high energy density needed, only small samples can be generated, with sizes typically of few tens to hundreds of micrometers. The timescale is

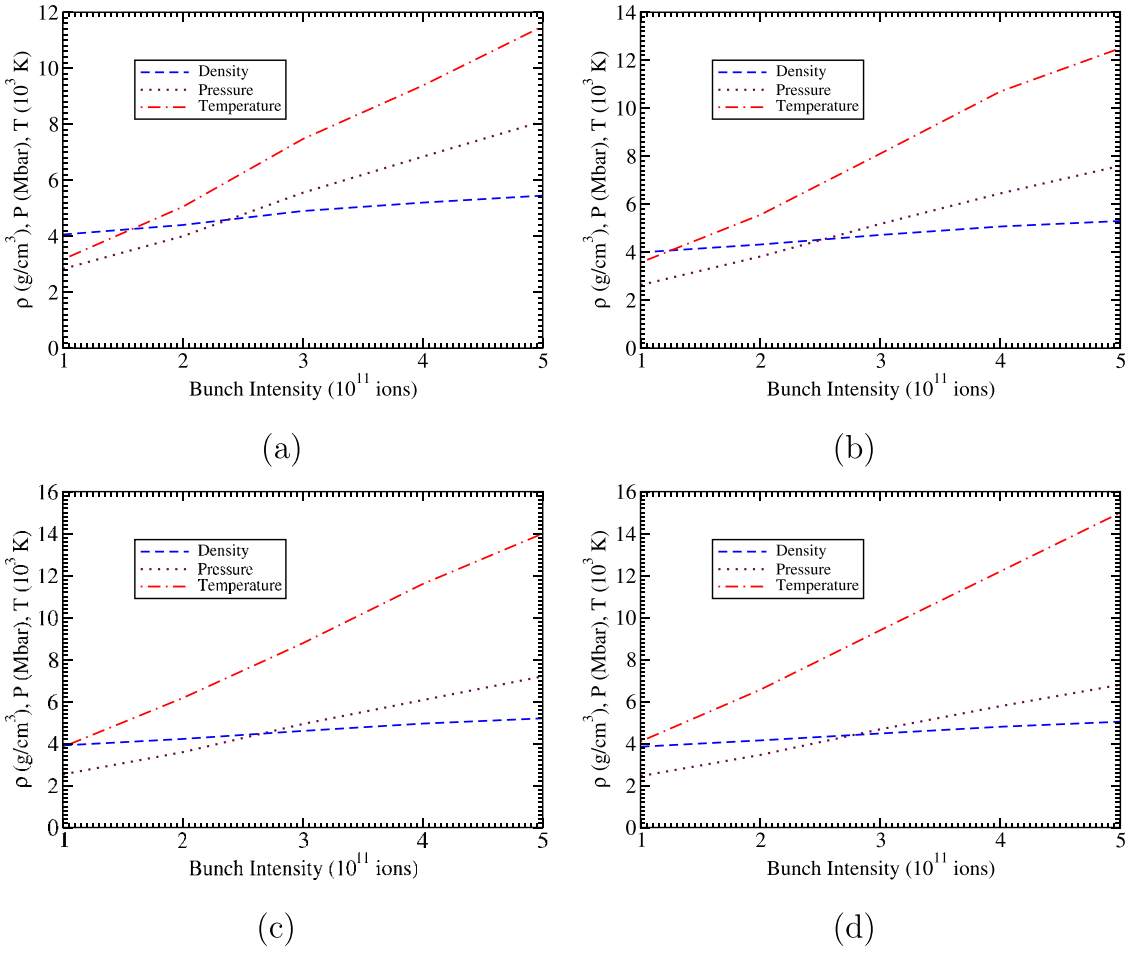

FIG. 23. Density, ρ, temperature, T, and pressure, P, vs bunch intensity, particle energy = 1.5 GeV/u, bunch length = 75 ns, sample radius, R_i = 0.2 mm, inner ring radius, R_1 = 0.4 mm, outer ring radius, R_2 = 1.4 mm; constant power step amplitude, A: (a) 25%, (b) 30%, (c) 35%, and (d) 40%.

given by the sound speed, typically in the range of tens to hundred km/s. As a consequence, measurements with high spatial and temporal resolution are required. Optical diagnostics are often used to measure thermal emission or determine the shock front velocity, but are restricted to visible surfaces. Here, laser-driven powerful x-ray sources, allow us to translate x-ray backlighting techniques well-established in medicine and materials science, such as x-ray radiographic imaging and x-ray diffraction, for the characterization of these short-lived extreme matter states. Hot plasmas at keV temperatures, heated by energetic laser pulses focused to intensities on order 10^{15} W/cm^2, emit powerful pulses of x-rays at photon energies around 10 keV, see, for example, Ref. 88. X-ray radiography enabled by these intense x-ray sources has become an indispensable diagnostic in many laboratory HED science experiments. In inertial confinement fusion experiments, it is routinely used to measure implosion velocity, symmetry and shell mass.[89] Measurements of shock velocity and mass density in shock experiments allows us to test EOS models,[90] recently accessing pressures of several hundred Mbar.[91,92]

Probing samples at high ρR, such as the compressed fusion fuel in the stagnation phase of ICF implosions, or the high densities achieved in LAPLAS-compressions, require higher x-ray energies to penetrate the samples and yield discernible contrast. Such powerful pulses of hard x-ray radiation are produced when micrometer-sized targets are irradiated with laser pulses at intensities exceeding 10^{18} W/cm^2. Here, the relativistic laser–matter interaction results in the acceleration of copious amounts of energetic (MeV) electrons, leading to the generation of x-rays in the target by characteristic line emission from inner-shell ionization[93] and bremsstrahlung.[94] While the conversion efficiency (the ratio of energy into x-ray photons, compared to the energy of the laser pulse) tends to be lower than the thermal emission from laser-heated plasmas, the x-ray spectrum reaches well into the range of several hundred keV, see, for example, Ref. 95. For this reason, many of the large laser-compression facilities worldwide have installed additional chirped pulse amplifier (CPA) laser systems for picosecond laser pulses with energies up to the kilo-Joule level,[96–98] enabling such hard x-ray radiographic capabilities. Likewise, at FAIR such a high-energy shortpulse laser system, the "Helmholtz-beamline," is currently under discussion to complement the unique compression capabilities with state-of-the-art HED diagnostic.

In order to assess the potential of this x-ray source for radiographic imaging of the LAPLAS implosions planned to be conducted at FAIR, we have performed simulations to generate realistic synthetic radiographic images to predict the achievable resolution and image noise. In these calculations we use the conversion efficiencies measured over a wide range of intensities at the PHELIX laser,[99] of 10^{-4} and 1.5×10^{-4} into the spectral ranges of 20–70 keV and 70–200 keV, respectively.[100] The spectral distribution has not been determined unambiguously, but the measurements are compatible with a 2-temperature Boltzmann-distribution composed of a colder (20–50 keV) and a hotter (300–500 keV) component, as was also inferred from similar experiments.[94] As a detector, we here assume a so-called imaging plate (IP) detector. IPs are frequently used media for recording ionizing radiation in HED experiments, mostly due to their versatility and ease of use and their robustness to the harsh environment typical for these experiments. For x-rays, a high detection efficiency is maintained up to several tens of keV, dropping significantly only beyond 100 keV.[101] We have modeled the detection probability and energy deposited per incident photon using the Monte Carlo package GEANT4.[102] The spatial resolution typically achieved with this type of detector is on order of 100 μm,[103] limited mostly by transverse light scattering in the phosphor layer during the readout process. In our simulations, we have applied a pixel size of 100 μm to include this detector resolution in the results. The calculated signal in each pixel contains the shot noise (Poisson distribution) from the finite number of photons emitted per spectral interval and into the solid angle subtended by the pixel. Furthermore, the photon absorption statistics in the sample as well as the quantum efficiency of the detection process is taken into account. We have validated our calculations comparing synthetic radiographic images with measurements taken at the PHELIX laser. Due to the experimental restrictions, here only 21.6 J of laser energy was used, focused onto the backlighter target, a 10 μm diameter tungsten wire. A radiographic image of three different thicknesses (13, 17, and 21 mm) of polymethyl methacrylate (PMMA) is shown in Fig. 24 (left). PMMA is chosen here as a surrogate for water. Being a low-Z material with a similar electron density, the absorption of 1 mm PMMA is almost identical to that of 0.8 mm of water over a wide range of photon energies. In the lineout (below) the average signal level behind the different samples can be seen. (Note: The unit PSL given in the images is the so-called photo-stimulated luminescence, the count value typically used for image plates. This value is proportional to the deposited dose over a wide dynamic range. For the simulations, we have used a conversion of 1 MeV/PSL, which we have measured using a well-characterized radioactive x-ray source.) Figure 24 (right) shows the synthetic radiograph generated from our simulation. As can be seen, both the signal level and the signal-to-noise ratio obtained in the experiment are well reproduced by the simulated images.

The same simulations have been performed to predict radiographic images from the LAPLAS compression targets outlined in Sec. VII A, case 1. For these simulations, however, we have assumed a laser pulse energy of 200 J, the projected baseline design parameter for the future laser facility. Both the x-ray source and the detector are on the cylinder axis of the LAPLAS-target, such that radiographic projections are along this axis. The source is located at a position of 10 mm in front of the target entrance. The detection plane is located on the other side at a distance of 1 m. This results in a geometric magnification factor of 75 (at the mid-plane of the target). A resolution element of 10 μm at the sample, thus, is magnified to 0.75 mm at the detector plane, a resolution that is easily achieved with imaging plates or other pixelated hard x-ray detectors. Source points are randomly distributed over an area of 10×10 μm to emulate the spatial extension of the x-ray source. This will lead to a blurring (extended point-spread-function) of the projected image corresponding to 10 μm at the object plane. Straight rays, originating at the source and terminated at the detector plane, are traced through the target density distributions from the hydrodynamic simulations. From this, we obtain the integrated ρR through the target for each location on the detector plane. The (spectrally dependent) absorption is then calculated using tabulated opacities from (XCOM). The use of cold opacities is justified as the x-ray

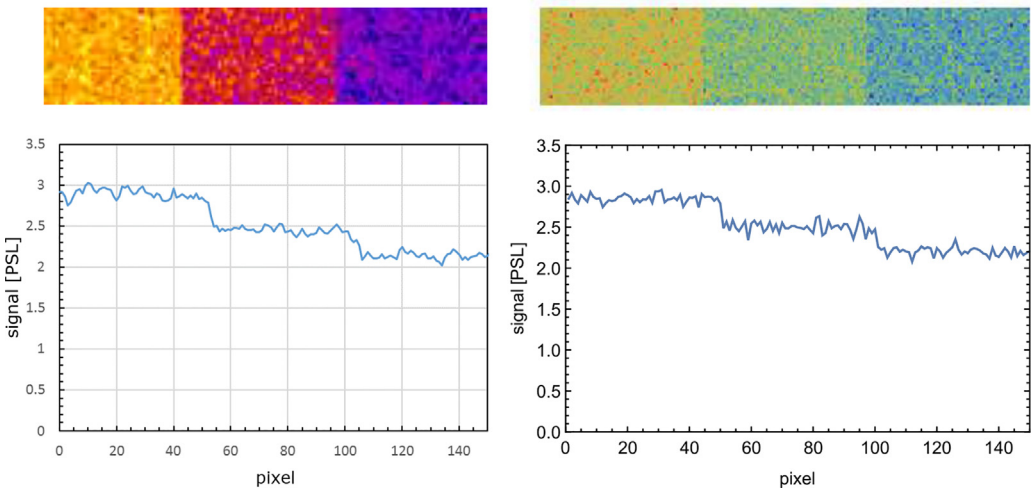

FIG. 24. (Left) Experimental image obtained at the PHELIX laser facility. The laser energy on the backlighter was 21.6 J, pixel size is 100 μm. The image (top) shows the raw data recorded on an imaging plate detector, the plot (bottom) is a 10 pixel wide lineout. (Right) Synthetic radiographic image.

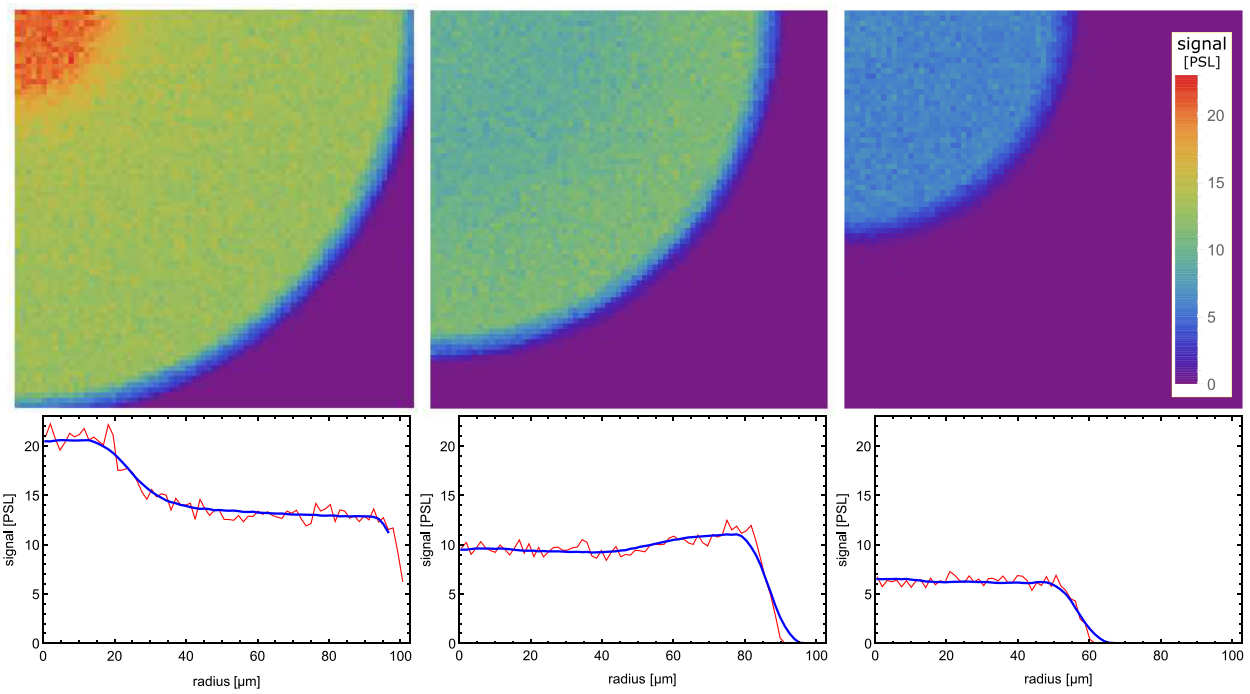

FIG. 25. (Top) Synthetic x-ray images at different times during the LAPLAS compression: (left) at 100 ns the converging first shock at r = 20 μm can be seen, (middle) at 105 ns around r = 50 μm, the weak shock reflected on the axis, and (right) around peak compression at 135 ns. (Bottom) Single-pixel lineout and a lineout convoluted with the 10 μm resolution limit due to the finite source size.

energies are well in the Compton-dominated regime where electrons are quasi-free and the attenuation depends only on the total electron density.[104] We note that the on-axis ion fluence is low enough to not damage the backlighter-target. Ions transmitted through the LAPLAS target can be further slowed down by several cm of low-Z material, which transmits the hard x-ray radiation. A 0.5 Tesla-m deflection magnet will deflect the ions sufficiently far off the axis to protect the imaging detector.

Figure 25 shows simulated radiographs for three different times during the implosions described in Sec. VII A. At t = 100 ns (left), the inwards moving first shock wave can be clearly observed at r ∼ 20 μm as a jump in the transmission at the transition from the shocked into the unshocked region. Also, the position of the tungsten tamper can be clearly seen. As time progresses (center), the tungsten wall moves inwards, radially compressing the sample. Measuring the position of the tungsten–water interface thus is a direct measure of the total sample volume. Finally (right), the fully compressed sample yields about 30% of the signal level of the uncompressed sample, which can still be measured accurately. The bottom panels in Fig. 25 show radial lineouts of the images. The red (thin) line represents a single-pixel lineout. From this we can infer a pixel-to-pixel signal-to-noise-ratio of approximately 10. When convoluting the image with the expected object resolution of 10 μm (as limited by the source size), the noise is further reduced, as shown by the blue (thick) line. The mass density can also be directly inferred from the signal strength. The absorption is a strictly monotonous function of the density. Therefore, a simultaneous radiograph of a calibration target with different thicknesses of the same material as the sample will provide a direct relation between density and signal strength. From these results, we conclude that radiographic imaging using a high-energy intense laser driven x-ray source will be a valuable diagnostic capability. It will be indispensable to monitor the target implosion performance. Measuring shock and interface velocity as well as mass density will allow us to access the equation-of-state of these extremely interesting matter states. Other x-ray diagnostic techniques, such as x-ray diffraction, requiring narrow-band radiation such as powerful K-alpha sources[93] could also be envisaged. This would give access to the microscopic structure, showing phase transitions to exotic new states such as superionic water, as was recently demonstrated in Ref. 105. In the future, spectrally resolved inelastic scattering techniques could provide access to the electronic structure and conductivities. For example, inelastic x-ray scattering has been shown to probe bound-free transitions,[106] while x-ray scattering in the collective regime has allowed to infer WDM conductivity from the shape and width of the plasmonic resonance.[107] Such measurements in the superionic ice regime would be of high interest as they might contribute to explain the anomalous magnetic fields found for the ice giants Uranus and Neptune.[108]

IX. CONCLUSIONS

This paper reports two-dimensional hydrodynamic simulations of compression of water in a multi-layered cylindrical target that is driven by an intense uranium beam. The beam parameters considered in this study are the design parameters of the beam that is to be delivered by the heavy ion synchrotron, SIS100, at the Facility for Antiprotons and Ion Research (FAIR). A wide range of beam and target parameters are considered to study the sensitivity of the results to uncertainties in the input parameters. Five different values of the bunch

intensity, including, 10^{11}, 2×10^{11}, 3×10^{11}, 4×10^{11}, and 5×10^{11} ions per bunch, are used. Two values for the sample radius, R_i, including 0.2 mm and 0.3 mm, respectively, are used. The corresponding sample mass is 1.26×10^{-3} g/cm and 2.83×10^{-3} g/cm, respectively. In the former case, two values of the inner ring radius of the annular focal spot, R_1, namely, 0.3 mm and 0.4 mm, are considered. These lead to payload mass of 3.01×10^{-2} g/cm and 7.24×10^{-2} g/cm, respectively. In the latter case, we use $R_1 = 0.4$ mm and 0.5 mm, which lead to payload mass of 4.22×10^{-2} g/cm and 9.65×10^{-2} g/cm, respectively. The simulations show that the results are quite insensitive to these significant variations in the sample and the payload mass for all the considered beam intensities. This indicates that the LAPLAS experimental scheme is stable to large uncertainties in the input parameters, which guarantees the success of the experiment. Moreover, the simulation results show that using the above beam parameter space, a wide range of extreme physical conditions relevant to the interior of water-rich planets, can be generated. The LAPLAS experiment will thus bring a wealth of information in the field of planetary physics.

ACKNOWLEDGMENTS

The authors would like to thank Martin French for useful discussions.

DATA AVAILABILITY

The data that support the finding of this study are available within the article.

REFERENCES

[1]See https://exoplanets.nasa.gov for exoplanet discoveries.
[2]D. Valencia, R. J. O'Connel, and D. Sasselov, ICARUS **181**, 545 (2006).
[3]D. Valencia, D. Sasselov, and R. J. O'Connel, Astrophys. J. **665**, 1413 (2007).
[4]D. Valencia, D. Sasselov, and R. J. O'Connel, Astrophys. J. **656**, 545 (2007).
[5]C. Sotin, O. Grasset, and A. Mocquet, ICARUS **191**, 337 (2007).
[6]D. C. Swift, J. G. Eggert, D. G. Hicks, S. Hamel, K. Caspersen, E. Schwegler, G. W. Collins, N. Nettelmann, and G. J. Ackland, Astrophys. J. **744**, 59 (2012).
[7]T. Duffy, N. Madhusudhan, and K. K. M. Lee, in *Treatise on Geophysics*, 2nd ed., edited by G. Schubert (Elsevier, Oxford, 2015), p. 149.
[8]M. J. Kuchner, Astrophys. J. **596**, L105 (2003).
[9]A. Leger, F. Selsis, C. Sotin, T. Guillot, D. Despois, D. Mawet, M. Ollivier, A. Labeque, C. Valette, F. Brachet *et al.*, ICARUS **169**, 499 (2004).
[10]D. Ehrenreich, A. L. des Etangs, J.-P. Beaulieu, and O. Grasset, Astrophys. J. **651**, 535 (2006).
[11]L. Zeng and D. Sasselov, Astrophys. J. **784**, 96 (2014).
[12]A. Ng, Int. J. Q. Chem. **112**, 150 (2012).
[13]P. D. Drake, Phys. Plasmas **16**, 055501 (2009).
[14]V. E. Fortov, *Extreme States of Matter* (Springer-Verlag, Heidelberg, 2016).
[15]N. A. Tahir, I. V. Lomonosov, B. Borm, A. R. Piriz, A. Shutov, P. Neumayer, V. Bagnoud, and S. A. Piriz, Astrophys. J. Suppl. Ser. **232**, 1 (2017).
[16]N. A. Tahir, A. Shutov, I. V. Lomonosov, A. R. Piriz, P. Neumayer, V. Bagnoud, and S. A. Piriz, Astrophys. J. Suppl. Ser. **238**, 27 (2018).
[17]N. A. Tahir, I. V. Lomonosov, B. Borm, A. R. Piriz, P. Neumayer, A. Shutov, V. Bagnoud, and S. A. Piriz, Contrib. Plasma Phys. **57**, 493 (2017).
[18]N. A. Tahir, A. Shutov, A. R. Piriz, P. Neumayer, I. V. Lomonosov, V. Bagnoud, and S. A. Piriz, Contrib. Plasma Phys. **59**, e201800135 (2019).
[19]W. F. Henning, Nucl. Instrum. Methods B **214**, 211 (2004).
[20]M. Durante, P. Indelicato, B. Johnson, V. Koch, K. Langanke, U. G. Miessner, E. Nappi, T. Nilsson, T. Stoehlker, E. Widmann *et al.*, Phys. Scr. **94**, 033001 (2019).
[21]B. Y. Tian and S. Stanley, Astrophys. J. **768**, 156 (2013).
[22]N. Nettelmann, U. Kramm, R. Redmer, and R. Neuhaeuser, Astron. Astrophys. **523**, A26 (2010).
[23]N. Nettelmann, K. Wang, J. J. Fortney, S. Hamel, S. Yellamilli, M. Bethkenhagen, and R. Redmer, ICARUS **275**, 107 (2016).
[24]M. Podolak, R. Helled, and G. Schubert, Mon. Not. R. Astron. Soc. **487**, 2653 (2019).
[25]L. Scheibe, N. Nettelmann, and R. Redmer, Astron. Astrophys. **632**, A70 (2019).
[26]T. Guillot and D. Gautier, in *Treatise on Geophysics*, 2nd ed., edited by G. Schubert (Elsevier, Oxford, 2015), p. 529.
[27]P. J. Spiller, R. Balss, A. Bleile, L. H. J. Bozyk, J. Ceballos Velasco, T. Eisel, E. S. Fisher, P. Fork, P. Huelsmann, M. Kauschke *et al.*, "Status of the FAIR synchrotron projects SIS18 upgrade and SIS100," in Proceedings of IPAC2014, Dresden, Germany, 2014.
[28]H. Geissel, H. Weick, M. Winkler, G. Muenzenberg, V. Chichkine, M. Yavor, T. Aumann, K. H. Behr, M. Boehner, A. Bruenle *et al.*, Nucl. Instrum. Methods B **204**, 71 (2003).
[29]M. Winkler, H. Geissel, H. Weick, B. Achenbach, K.-H. Behr, D. Boutin, A. Bruehle, M. Gleim, W. Hueller, C. Karagiannis *et al.*, Nucl. Instrum. Methods B **266**, 4183 (2008).
[30]N. A. Tahir, V. Kim, A. Matveichev, A. V. Ostrik, A. V. Shutov, I. V. Lomonosov, A. R. Piriz, J. J. Lopez Cela, and D. H. H. Hoffmann, Laser Part. Beams **26**, 273 (2008).
[31]C. Schwarz and PANDA Collaboration, J. Phys.: Conf. Ser. **374**, 012003 (2012).
[32]T. Stöhlker, V. Bagnoud, K. Blaum, A. Blazevic, A. Braeuning-Dermain, M. Durante, F. Herfurth, M. Lestinsky, Y. Litvinov, S. Neff *et al.*, Nucl. Instrum. Methods B **365**, 680 (2015).
[33]H. K. Mao and R. J. Hemley, Rev. Mod. Phys. **66**, 671 (1994).
[34]C. Narayan, H. Luo, and A. L. Ruoff, Nature **393**, 46 (1998).
[35]R. Boehler, Rev. Geophys. **38**, 221, https://doi.org/10.1029/1998RG000053 (2000).
[36]A. V. Altschuler, R. F. Trunen, K. K. Krupnikov, and N. V. Panov, Phys.-Usp. **39**, 539 (1996).
[37]M. van Thiel, Compendium of Shock Wave Data, Report No. UCRL-50108, 1977.
[38]V. E. Fortov, V. Y. Ternovoi, M. V. Zernokletov, M. A. Mochalov, A. L. Michailov, A. S. Filimonov, A. A. Pyalling, V. B. Mintsev, V. K. Gryaznov, and I. L. Iosilevski, J. Exp. Theor. Phys. **97**, 259 (2003).
[39]M. D. Knudson, D. L. Hanson, J. E. Bailey, C. A. Hall, J. R. Asay, and W. W. Anderson, Phys. Rev. Lett. **87**, 225501 (2001).
[40]T. Loewer, R. Sigel, K. Eidmann, B. Foeldes, S. Hueller, J. Massen, G. D. Tsakiris, S. Witkowski, W. Preuss, H. Nishimura *et al.*, Phys. Rev. Lett. **72**, 3186 (1994).
[41]R. Cauble, D. W. Fillion, T. J. Hoover, N. C. Holmes, J. D. Kilkenny, and R. W. Lee, Phys. Rev. Lett. **70**, 2102 (1993).
[42]M. Koenig, B. Faral, J. M. Boudenne, D. Batani, A. Benuzzi, S. Bossi, C. Remond, J. P. Perrine, M. Temporal, and S. Atzeni, Phys. Rev. Lett. **74**, 2260 (1995).
[43]A. S. Vladimirov, N. P. Voloshin, V. N. Nogin, A. V. Petrovtsev, and V. A. Simoneko, J. Exp. Theor. Phys. **39**, 82 (1984).
[44]N. A. Tahir, D. H. H. Hoffmann, J. A. Maruhn, P. Spiller, and R. Bock, Phys. Rev. E **60**, 4715 (1999).
[45]N. A. Tahir, A. Kozyreva, P. Spiller, D. H. H. Hoffmann, and A. Shutov, Phys. Rev. E **63**, 036407 (2001).
[46]N. A. Tahir, A. Adonin, C. Deutsch, V. E. Fortov, N. Grandjouan, B. Geil, V. Grayaznov, D. H. H. Hoffmann, M. Kulish, I. V. Lomonosov *et al.*, Nucl. Instrum. Methods A **544**, 16 (2005).
[47]N. A. Tahir, P. Spiller, A. Shutov, I. V. Lomonosov, V. Grayaznov, A. R. Piriz, G. Wouchuk, C. Deutsch, V. E. Fortov, D. H. H. Hoffmann *et al.*, Nucl. Instrum. Methods A **577**, 238 (2007).
[48]N. A. Tahir, P. Spiller, S. Udrea, O. D. Cortazar, C. Deutsch, V. E. Fortov, V. Gryazanov, D. H. H. Hoffmann, I. V. Lomonosov, P. Ni *et al.*, Nucl. Instrum. Methods B **245**, 85 (2006).
[49]N. A. Tahir, A. Shutov, D. Varentsov, P. Spiller, S. Udrea, D. H. H. Hoffmann, I. V. Lomonosov, J. Wieser, M. Kirk, A. R. Piriz *et al.*, Phys. Rev. ST Accel. Beams **6**, 020101 (2003).

[50]N. A. Tahir, B. Goddard, V. Kain, R. Schmidt, A. Shutov, I. V. Lomonosov, A. R. Piriz, M. Temporal, D. H. H. Hoffmann, and V. E. Fortov, J. Appl. Phys. **97**, 083532 (2005).
[51]N. A. Tahir, T. Stoehlker, A. Shutov, I. V. Lomonosov, V. E. Fortov, M. French, N. Nettelmann, R. Redmer, A. R. Piriz, C. Deutsch *et al.*, New J. Phys. **12**, 073022 (2010).
[52]N. A. Tahir, A. Shutov, A. P. Zharkov, A. R. Piriz, and T. Stoehlker, Phys. Plasmas **18**, 032704 (2011).
[53]N. A. Tahir, P. Neumayer, A. Shutov, A. R. Piriz, I. V. Lomonosov, V. Bagnoud, S. A. Piriz, and C. Deutsch, Contrib. Plasma Phys. **59**, e201800143 (2019).
[54]U. N. Funk, R. Bock, M. Dornik, M. Geissel, M. Stetter, S. Stoewe, N. A. Tahir, and D. H. H. Hoffmann, Nucl. Instrum. Methods A **415**, 68 (1998).
[55]A. R. Piriz, J. J. Lopez Cela, M. C. Serna Mareno, N. A. Tahir, and D. H. H. Hoffmann, Laser Part. Beams **24**, 275 (2006).
[56]S. A. Piriz, A. R. Piriz, and N. A. Tahir, Phys. Rev. E **95**, 053108 (2017).
[57]S. A. Piriz, A. R. Piriz, and N. A. Tahir, Phys. Fluids **30**, 111703 (2018).
[58]S. A. Piriz, A. R. Piriz, and N. A. Tahir, J. Fluid Mech. **867**, 1012 (2019).
[59]S. A. Piriz, A. R. Piriz, and N. A. Tahir, Phys. Rev. E **97**, 043106 (2018).
[60]J. J. Lopez Cela, A. R. Piriz, M. C. Serna Moreno, and N. A. Tahir, Laser Part. Beams **24**, 427 (2006).
[61]J. J. Barnard, J. Armijo, R. M. More, A. Frieman, I. Kaganovich, B. G. Logan, M. M. Marinak, G. E. Penn, A. B. Sefkow, P. Santhanam *et al.*, Nucl. Instrum. Methods A **577**, 275 (2007).
[62]N. A. Tahir, C. Deutsch, V. E. Fortov, V. Gryazanov, D. H. H. Hoffmann, M. Kulish, I. V. Lomonosov, V. Mintsev, P. Ni, D. Nikolaev *et al.*, Phys. Rev. Lett. **95**, 035001 (2005).
[63]N. A. Tahir, A. Shutov, I. V. Lomonosov, A. R. Piriz, G. Wouchuk, C. Deutsch, D. H. H. Hoffmann, and V. E. Fortov, High Energy Density Phys. **2**, 21 (2006).
[64]N. A. Tahir, P. Neumayer, I. V. Lomonosov, A. Shutov, V. Bagnoud, A. R. Piriz, S. A. Piriz, and C. Deutsch, Phys. Rev. E **101**, 023202 (2020).
[65]K. Schoenberg, V. Bagnoud, A. Blazevic, V. E. Fortov, D. O. Gerike, A. Golubev, D. H. H. Hoffmann, D. Kraus, I. V. Lomonosov, V. Mintsev *et al.*, Phys. Plasmas **27**, 043103 (2020).
[66]R. O. Bangerter, J. W. K. Mark, and A. R. Thiessen, Phys. Lett. A **88**, 225 (1982).
[67]G. R. Magelssen, Nucl. Fusion **24**, 1527 (1984).
[68]C. Deutsch, Ann. Phys. **11**, 1 (1986).
[69]B. G. Logan, L. J. Perkins, and J. J. Barnard, Phys. Plasmas **15**, 072701 (2008).
[70]A. R. Piriz and M. M. Sanchez, Phys. Plasmas **5**, 2721 (1998).
[71]K. A. Long and N. A. Tahir, Phys. Lett. A **91**, 451 (1982).
[72]N. A. Tahir and K. A. Long, Atomkernenerg.-Kerntech. **40**, 157 (1982).
[73]N. A. Tahir and K. A. Long, Laser Part. Beams **2**, 371 (1984).
[74]N. A. Tahir and K. A. Long, Phys. Fluids **29**, 1282 (1986).
[75]N. A. Tahir and K. A. Long, Z. Phys. A **325**, 99 (1986).
[76]K. A. Long and N. A. Tahir, Nucl. Fusion **26**, 555 (1986).
[77]A. R. Piriz, M. Temporal, J. J. Lopez Cela, N. A. Tahir, and D. H. H. Hoffmann, Plasma Phys. Controlled Fusion **45**, 1733 (2003).
[78]S. Minaev, N. Alexeev, A. Golubev, D. H. H. Hoffmann, T. Kulevoy, B. Sharkov, A. Sitnikov, N. A. Tahir, and D. Varentsov, Nucl. Instrum. Methods A **620**, 99 (2010).
[79]M. Temporal, J. J. Lopez Cela, A. R. Piriz, N. Grandjoun, N. A. Tahir, and D. H. H. Hoffmann, Laser Part. Beams **23**, 137 (2005).
[80]S. A. Piriz, A. R. Piriz, and N. A. Tahir, Phys. Rev. E **100**, 063104 (2019).
[81]S. K. Godunov, Mat. Sbornik **47**, 271 (1959).
[82]V. E. Fortov, B. Goel, C. D. Munz, A. L. Ni, A. V. Shutov, and O. Y. Vorobiev, Nucl. Sci. Eng. **123**, 169 (1996).
[83]J. F. Ziegler, J. P. Biersack, and U. Littmark, *The Stopping and Ranges of Ions in Solids* (Pergamon Press, New York, 1996).
[84]I. V. Lomonosov, Laser Part. Beams **25**, 567 (2007).
[85]V. E. Fortov and I. V. Lomonosov, Phys. Usp. **57**, 219 (2014).
[86]A. S. Khan and S. Huang, *Continuous Theory of Plasticity* (J. Wiley & Sons, Inc., New York, 1995).
[87]P. L. Stanford and J. D. Johnson, "SESAME: The Los Alamos National Laboratory EOS data," Report No. LA-UR-92-3407, 1984.
[88]L. E. Ruggels, J. L. Porter, P. K. Rambo, W. W. Simpson, M. F. Vargas, C. R. Bennet, and I. C. Smith, Rev. Sci. Instrum. **74**, 2206 (2003).
[89]J. R. Rygg, O. S. Jones, J. E. Field, M. A. Barrios, L. R. Benedetti, G. W. Collins, D. C. Eder, M. J. Edwards, J. L. Kline, J. J. Kroll *et al.*, Phys. Rev. Lett. **112**, 195001 (2014).
[90]G. W. Collins, L. B. Da Silva, P. Celliers, D. M. Gold, M. E. Foord, R. J. Wallace, A. Ng, S. V. Weber, K. S. Budil, and R. Cauble, Science **281**, 1178 (1998).
[91]T. Doepner, D. C. Swift, A. L. Kritcher, B. Bachmann, G. W. Collins, D. A. Chapman, J. Hawreliak, D. Kraus, J. Nilsen, S. Rothman *et al.*, Phys. Rev. Lett. **121**, 025001 (2018).
[92]A. L. Kritcher, D. C. Swift, T. Doepner, B. Bachman, L. X. Benedict, G. W. Collins, J. L. DuBois, F. Eisner, G. Fontaine, J. A. Gaffney *et al.*, Nature **584**, 51 (2020).
[93]H.-S. Park, B. R. Maddox, E. Giraldez, S. P. Hatchett, L. T. Hudson, N. Izumi, M. H. Key, S. L. Pape, A. J. MacKinnon, A. C. MacPhee *et al.*, Phys. Plasmas **15**, 072705 (2008).
[94]C. D. Chen, P. K. Patel, D. S. Hey, A. J. MacKinnon, M. H. Key, K. U. Akli, T. Bartal, F. N. Beg, S. Chawla, H. Chen *et al.*, Phys. Plasmas **16**, 082705 (2009).
[95]R. Tommasini, C. Bailey, D. K. Bradley, M. Bowers, H. Chen, J. M. Di Nicola, P. D. Nicola, G. Cururangan, G. N. Hall, C. M. Hardy *et al.*, Phys. Plasmas **24**, 053104 (2017).
[96]J. K. Crane, G. Tietbohi, P. Arnold, E. S. Bliss, C. Boley, G. Britten, G. Brunton, W. Clark, J. W. Dawson, S. Fochs *et al.*, J. Phys.: Conf. Ser. **244**, 032003 (2010).
[97]D. N. Maywar, J. H. Kelly, L. J. Waxer, S. F. B. Morse, I. A. Begishev, J. Bromage, C. Dorrer, J. L. Edwards, L. Folnsbee, M. J. Guardalben *et al.*, J. Phys.: Conf. Ser. **112**, 032007 (2008).
[98]J. Schwarz, P. Rambo, M. Geissel, A. Edens, I. Smith, E. Brambrink, M. Kimmel, and B. Atherton, J. Phys.: Conf. Ser. **112**, 032020 (2008).
[99]V. Bagnoud, B. Aurand, A. Blazevic, S. Borneis, C. Bruske, B. Ecker, U. Eisenbarth, J. Fils, A. Frank, E. Gaul *et al.*, Appl. Phys. B **100**, 137 (2010).
[100]B. Borm, D. Khaghani, and P. Neumayer, Phys. Plasmas **26**, 023109 (2019).
[101]A. L. Meadowcroft, C. D. Bentley, and E. N. Stott, Rev. Sci. Instrum. **79**, 113102 (2008).
[102]K. Li, B. Borm, F. Hug, D. Khaghani, B. Lother, D. Savran, N. A. Tahir, and P. Neumayer, Laser Part. Beams **32**, 631 (2014).
[103]G. Fiksel, F. Marshall, C. Mileham, and C. Stoeckl, Rev. Sci. Instrum. **83**, 086103 (2012).
[104]R. Tommasini, S. P. Hatchett, D. S. Hey, C. Iglesias, N. Izumi, J. A. Koch, O. L. Landen, A. J. MacKinnon, C. Source, J. A. Delettrez *et al.*, Phys. Plasmas **18**, 056309 (2011).
[105]M. Millot, F. Coppari, J. R. Rygg, A. C. Barrios, S. Hammel, D. C. Swift, and J. H. Eggert, Nature **569**, 251 (2019).
[106]L. B. Fletcher, A. L. Kritcher, A. Park, T. Ma, T. Dopner, C. Fortmann, L. Divol, O. S. Jones, O. L. Landel, H. A. Scott *et al.*, Phys. Rev. Lett. **112**, 145004 (2014).
[107]B. B. L. Witte, L. B. Fletcher, E. Galtier, E. Gamboa, H. J. Lee, U. Zastaru, R. Redmer, S. H. Glenzer, and P. Sperling, Phys. Rev. Lett. **118**, 225001 (2017).
[108]H. F. Wilson, M. L. Wong, and B. Militzer, Phys. Rev. Lett. **110**, 151102 (2013).